Influence of water on deformation and failure of gypsum rock

C. Caselle, P. Baud, A.R.L. Kushnir, T. Reuschlé, S.M.R. Bonetto

Influence of water on deformation and failure of gypsum rock

C. Caselle[1,*], P. Baud[2], A.R.L. Kushnir[2], T. Reuschlé[2], S.M.R. Bonetto[1]

1 - Department of Earth Sciences - DST, Università degli Studi di Torino, Torino, Italy

2 - Université de Strasbourg, CNRS, Institut Terre et Environnement de Strasbourg, UMR 7063, 5 rue René Descartes, Strasbourg F-67084, France

**corresponding author: chiara.caselle@unito.it, 011/ 6705139 – Via Valperga Caluso 35, Torino (TO), 10125, Italy*

Abstract

While water is known to significantly reduce the strength of rocks, there remains a paucity of data on water-weakening of gypsum. Here, we quantify water-weakening in a natural gypsum facies from Monferrato (Italy) by performing experiments on nominally dry, oil-saturated, and water-saturated samples. Uniaxial and conventional triaxial experiments revealed significant water-weakening in Monferrato gypsum as well as a strong strain-rate dependence of uniaxial compressive strength. Moreover, uniaxial creep tests showed significant time-dependent deformation in samples saturated with sulphate over-saturated water, but not in dry and oil-saturated samples. The creep phenomenology is similar to that observed in other rock types and is consistent with stress-corrosion microcracking, which is supported by our microstructural observations. However, we systematically recorded more inelastic strain in samples deformed at low strain-rates suggesting that additional mechanisms were also active. Comparing our new data on short-term strength with published results for other rock types, we conclude that, when saturated with water in equilibrium with the rock, weakening in gypsum is not notably higher than in other rocks and is partially due to a reduction of fracture toughness in the presence of water.

Keywords

Branching selenite gypsum, mechanical strength, creep, microcracking, kinking, dissolution

1. Introduction

Gypsum is an evaporitic mineral that plays an important role in several areas of structural geology and civil engineering. It is involved in orogenetic tectonics, influences basin dynamics, and is associated with many economic activities including oil exploration, mining, and waste repositories (e.g. Heard & Ruby 1986; de Meer and Spiers, 1999; Cristallini & Ramos 2000; Zucali et al., 2010,

Liang et al., 2012). In particular, underground mining excavations in gypsum have often resulted in roof collapses, pillar failures, water inrushes, and generation of surface subsidence, especially after unexpected water circulation and in abandoned or old underground sites (e.g. Bonetto et al. 2008; Wang et al., 2008; Sadeghiamirshahidi and Vitton 2019).

From a crystallographic point of view, gypsum is a layered mineral, with pairs of adjacent sheets of Ca^{2+} and $(SO_4)^{2-}$ tetrahedra separated by double-sheets of water molecules (Figure 1a), resulting in a pervasive cleavage in gypsum crystals (Figure 1b).

Figure 1

This anisotropy at the crystal scale controls some of the principal physical features of gypsum, including the mineral rheology, as first suggested by Craker and Schiller (1962). In that study, the authors experimentally tested the deformation of a single gypsum crystal with a three-point loading system, showing that, when the applied stress is perpendicular to the mineral cleavage (010 plane) the crystal bends and significant plastic deformation may be observed even at relatively fast strain rates. When, on the other hand, the stress is applied parallel to the cleavage, the crystal fractures before any detectable bending occurs.

At the rock scale, the variability of gypsum facies all over the world (with differences in grain size, porosity, gypsum content and rock structure) results in a broad range of values of mechanical strength, both under uniaxial and triaxial loading conditions (e.g. Papadopoulos et al., 1994; Yilmaz, 2007; Caselle et al., 2019a-b). Under triaxial loading conditions, gypsum may exhibit micro-plasticity resulting from grain kinking (Brantut et al. 2011, Caselle et al., 2020a-b).

The solubility of gypsum in water is 0.015 mol/kg H_2O, which is significantly higher than for several other minerals. As such, the mechanical properties of gypsum are very sensitive to the presence of water, which may cause important weathering and weakening effects. Auvray et al. (2004) observed that the external portions of gypsum pillars in an abandoned underground mine, being more exposed to the humid atmosphere of the drifts, showed evidence of dissolution and corrosion using scanning electron microscopy in secondary electron acquisition mode (SEM-SE). In agreement with these observations, they measured significant changes in material properties (e.g. increase in porosity and decreases in seismic wave velocity and mechanical strength) from the core to the external surface of the pillars. In terms of uniaxial compressive strength, Yilmaz (2010) measured a weakening of about 50% in water-saturated gypsum samples compared to dry samples. The decrease of mechanical properties (strength, elastic moduli) was also observed by Castellanza et al. (2008) and Castellanza et al. (2010), who reported on the stability assessment of an abandoned underground gypsum quarry,

proposing an evaluation of pillar stability based on the deteriorating effect of water. The experimental investigation by Liang et al. (2012) introduced an additional element, considering the effect of temperature and NaCl in the soaking brine. Their results suggest a positive correlation between weakening and NaCl concentration and temperature during saturation. Zhu et al. (2019)'s multiscale investigation of the phenomenon suggests that the reduction of mechanical strength results from the hydrolysing and weakening of crystal bonds at microcrack tips and is exacerbated by the continuous increase of immersion time.

While there is clear evidence of water-weakening in gypsum, the processes that result in this strength reduction remain unclear. Previous studies on water-weakening in different rock types have concluded that various physical mechanisms could contribute to water-weakening in rocks (Baud et al., 2000, Nicolas et al., 2016, Noel et al., 2021, Geremia et al., 2021): 1) A reduction of the surface energy and of the fracture toughness in the presence of water, sometimes called the Rhebinder effect (see for example Røyne et al., 2011); 2) Stress corrosion effects observed in most rock types (Brantut et al., 2014a-b); 3) intergranular pressure solution (Croizé et al., 2013); 4) Capillary effects due to the presence of water, even in a nominally dry rock (Delage et al., 1996; Risnes et al., 2005); and 5) Dissolution at the grain surfaces (Ciantia et al., 2015). Additionally, the mechanical effect of water could result in complex effective pressure behavior, as observed for example in clayey sandstone and dual porosity carbonates (Meng et al., 2020).

The microstructures produced in gypsum during its dissolution in water have been investigated using SEM (e.g. Yu et al., 2016) and X-ray computed microtomography (CT, e.g. Meng et al., 2018). Yu et al. (2016), in particular, described a process of crystal splitting along cleavage during dissolution, in accordance with experimental evidence that dissolution on (010) crystallographic faces occurs at a higher rate than in other crystallographic directions (Fan and Teng, 2007).

Water has also been observed to influence the creep behaviour of gypsum. De Meer and Spiers (1995, 1997, 1999) measured a clear difference in creep behaviour of gypsum powder samples: dry and oil saturated samples exhibited little to no creep, while under water saturated conditions, samples exhibited significant creep. Based on their experimental results, the authors proposed a creep model driven by pressure solution but also suggested that precipitation of gypsum on the pore walls acts as a rate-limiting mechanism. More recently, Hoxha et al. (2005, 2006) measured a clear dependence of creep strain rate of gypsum rock samples on relative humidity. Their experimental results demonstrated strong time-dependent and humidity-dependent dilatancy, that the authors considered as an indication of a damage-like mechanism. Following the authors' interpretation, this mechanism would be unrelated to the growth of new cracks and would consist in the creation of a water layer

along the crystal contacts that would ease the sliding between one crystal and another. According to the authors, these water layers would be created by water molecules from both the humid atmosphere and the crystalline structure of gypsum that, when the material is under stress, migrate from their sites to the pores of the rock. However, this complex mechanism involves gypsum dehydration that is difficult to obtain under the experimental conditions investigated by Hoxha et al. (2005; 2006). A clear explanation of the micro-mechanical mechanisms involved in creep in gypsum rock is therefore still needed.

The impact of water on the mechanical strength and physical properties of gypsum rock is particularly relevant to underground excavation (Ramon et al., 2021). Gypsum quarries are often located below the static level of the groundwater table and thus require continuous water pumping to permit excavation of drifts. The end of quarry activity, coinciding with the interruption of de-watering operations and the re-establishment of the original water level, results in the re-saturation of the gypsum body. Under these conditions, the water fills the connected porosity of the rock, influencing both short-term and long-term stability of the underground quarries. For these reasons, the current study aims to analyse the micromechanical mechanisms that control the changes in mechanical response of gypsum rock in the presence of water. We use a natural gypsum rock facies (i.e. branching selenite) that is exploited in underground environments in several areas of the Mediterranean basin. Our experimental investigation also aims to quantify the specific effect of water-gypsum chemical interactions, comparing the results obtained by saturating the material with water and with a non-reactive oil. Hence, mechanical tests were performed under dry, oil-saturated, and water-saturated conditions. Our investigation includes uniaxial compression tests, uniaxial creep tests, and conventional triaxial experiments. Microstructural analysis of deformed samples was performed to describe the mechanisms involved in gypsum deformation and failure.

2. Tested material and sample preparation

All our tests were performed on a Miocene microcrystalline gypsum in branching selenite facies (sensu Lugli et al., 2010). Samples were cored in the Monferrato domain of the Tertiary Piedmont Basin (TPB), a complex sedimentary basin located on the inner side of the SW Alps arc that occupied large areas of Piedmont (NW Italy) from the Upper Eocene to the end of the Miocene (Clari et al., 1995; Piana and Polino, 1995; Dela Pierre et al., 2011). The sediments of the TPB stratigraphically overlie a complex tectonic wedge of Alpine, Ligurian and Adria basement units juxtaposed in response to the collision between the European and Adria plates (e.g. Rossi et al 2009). The Cenozoic sediments are presently exposed in the southern (Langhe, Alto Monferrato and Borbera Grue domains) and the northern (Torino Hill–Monferrato arc) sectors of the TPB. The relationships

between the two outcropping belts are masked by the Pliocene to Holocene deposits of the Savigliano and Alessandria basins, but are well imaged by seismic profiles (Bertotti et al 2009). Thick gypsum bodies from the Messinian Salinity Crisis (late Miocene) are observed and described in the Monferrato and Langhe domains (Figure 2a).

The stratigraphic succession of the test site comprises deep-sea marls overlayed by a geological unit that includes a thick evaporitic succession that counts 13 gypsum – marl cycles (Dela Pierre et al., 2016). The material tested for the present study was sampled from the fourth cycle (the 6th from the onset of the Messinian Salinity Crisis), that corresponds to the appearance of the so-called "branching selenite facies" (Lugli et al. 2010). This layer, that has a thickness of about 10 m, is recognized in the geological literature as the "Sturani Key Bed" (SKB) (Dela Pierre et al., 2011).

At the sample scale, branching selenite facies are organized in nodular aggregates consisting of mm- to cm-sized gypsum crystals (Figure 2d). In the aggregates, the gypsum crystals are closely interlocked, creating a dense structure; their habit is usually prismatic and several of them show twinning. Most of the crystals show the presence of both fluid and solid inclusions (Natalicchio et al. 2021, Cipriani et al. 2021). These nodules are immersed in a fine matrix organized in laminae composed of gypsum, calcite and terrigenous minerals (mainly clays, quartz and feldspars). A single dominant orientation of the elongated gypsum crystals in nodules is apparent (Caselle et al. 2020c – Figure 2c). The gypsum content of this rock generally ranges between 85 and 95 wt% (Caselle et al. 2019a).

Figure 2

2.1 Sampling and porosity determination

Mechanical tests were performed on 77 cylindrical samples (height: 40 mm; diameter: 20 mm – Figure 2b), re-sampled from two bigger 80 mm in diameter pieces of borehole core. All samples were cored in the vertical (i.e. borehole-parallel) direction from both core pieces. Both core pieces are from the same axial borehole, drilled as part of a survey campaign included in the exploitation plane of an underground quarry. The vertical borehole is oriented perpendicular to the sub-horizontal stratification and main sedimentary discontinuities; the borehole crosses the branching selenite layer between 77 m to 87 m of depth. The two core pieces used in this study were drilled between 82.4 to 82.9 m (Core 1) and 78.0 to 78.7 m (Core 2) depth.

The porosity of all 40mm by 20mm samples was measured using a helium pycnometer, following EN ISO 17892-3:2016 recommendations. Measured values of porosity range between 0.034 and 0.098, solid density ranges between 2.33 and 2.43 g/cm^3 and bulk density is between 2.15 and 2.27

163 g/cm^3. The values of porosity and bulk density are shown in Figure 3. Density decreases linearly with
164 the porosity suggesting that the solid density was about the same in the studied cores, and therefore
165 that the mineralogical composition of all our samples was comparable. In detail, a comparison of
166 these measurements with the theoretical curve of pure gypsum (solid density ρ_s = 2.4 g/cm^3)
167 confirmed the presence of other minerals beside gypsum in the studied rock, as well as the lower
168 density of Core 1 with respect to Core 2. This is supported by the X-ray powder diffraction (XRPD)
169 analysis of non-gypsum portions of Core 1 and Core 2. Since the XRPD analyses were specifically
170 performed to characterize non-gypsum mineralogical content, the material was ground using a mortar
171 and pestle and dissolved in water, ensuring that the solid/water ratio reached a concentration of
172 calcium sulfate lower than gypsum solubility (2 g/l at 20°C). After 24 hours, the solution was filtered
173 and the residual solid portion was smeared on glass slides. This sample preparation method allowed
174 XRPD characterization of the insoluble minerals without the interference of the gypsum diffraction
175 pattern. Analyses were performed using a Miniflex 600 diffractometer, with lambda value of 1.54
176 angstrom and 2-theta ranging from 0 to 50 (complete procedure and data may be found in Caselle et
177 al, 2022). Results (Figure 3b) show that only calcite is present in Core 2 (blue line), while Core 1 (red
178 line) also contains clay minerals, calcite and minor quartz and feldspars, consistent with the higher
179 density of Core 2 with respect to Core 1 (complete procedure and data may be found in Caselle et al,
180 2022).

181 Gas permeability was measured on three samples, selected on the basis of the connected porosity
182 (maximum, minimum and mean values in the investigated dataset), using the pulse decay method
183 detailed by Heap et al. (2017). Results show that permeability ranged between $2 \cdot 10^{-17}$ m^2 and less
184 than 10^{-19}m^2.

185 **Figure 3**

186 *2.2 Water saturation*

187 Due to the high solubility of gypsum, it was important to ensure that our water-saturated samples
188 were in equilibrium with the saturating fluid over long periods of time, in particular during the
189 mechanical tests performed at low strain rates and under creep conditions. To do this, the saturation
190 process was performed with a gypsum-water solution in chemical equilibrium with the material. To
191 create this gypsum-saturated water solution, we placed gypsum powder and rock offcuts in distilled
192 water. Dissolution was monitored by measuring the electrical conductivity of the solution over time;
193 after 10 days, a stable value of 1.8 mS/cm was obtained. This solution, *a priori* at equilibrium, was
194 then used to saturate the samples. Samples were vacuum-saturated and then left in the solution for a
195 period of at least two weeks. The conductivity, monitored throughout the saturation period, remained
196 stable at 1.8 mS/cm.

197 *2.3 Oil saturation*

198 Our experimental program also included compression of oil-saturated samples, aiming to examine
199 the inert reaction between gypsum and an apolar fluid. Despite the absence of a dissolution process,
200 the saturation with dearomatized oil produced an intense red discolouration on the surface of the
201 samples (Figure 4a). This red discolouration was particularly concentrated along the fine-grained
202 layers of the branching selenite structure and persisted even after the samples were allowed to
203 desaturate under ambient laboratory conditions (i.e. dry out), as shown in Figure 4b (after a period of
204 about one month). In order to identify the source of the red discolouration, one of these oil-saturated
205 samples was analysed using SEM energy dispersive X-ray spectroscopy (EDS). The resulting
206 compositional maps (obtained on one of the circular faces of the sample) show the classical features
207 of branching selenite facies, with 1 to 2 mm sulphate crystals (in Figure 4c, gypsum in green and
208 celestine in orange), carbonate minerals of about 0.1 mm (in blue) and a finer, siliceous matrix (in
209 red on the map in Figure 4c). The areas of red discolouration in the macroscopic samples correspond
210 to the siliceous matrix. Point EDS analyses showed the presence of Si, Al, Mg, Na and minor K and
211 Fe (Figure 4d) that indicate the presence of multi-layered clay minerals (mainly illite and smectite).
212 This suggests that the red discolouration results from the absorption of dearomatized oil in the
213 swelling layers of the clay minerals. To confirm if the dearomatized oil was absorbed by the clay
214 minerals, an oil-saturated sample was heated to 350°C (i.e. the decomposition temperature of
215 smectite). Following heat treatment, the red portions of the sample turned to black, confirming an
216 expulsion of the red/dearomatized oil due to the collapse of the clay structure (Figure 4e).

217 **Figure 4**

218 **3. Experimental procedures**

219 *3.1 Uniaxial compression*

220 23 uniaxial compression tests were performed at the Institut Terre et Environnement de Strasbourg
221 (ITES; the Strasbourg Institute for the Earth and the Environment), using a servo-controlled uniaxial
222 press. Axial displacement was measured throughout the test using an LVDT with an accuracy of
223 ±0.15 μm, while the axial force was measured with an accuracy of ±9 N (corresponding to an accuracy
224 of the applied stress of ±0.03 MPa). Details about this set-up can be found in Heap et al. (2014). All
225 the tests were performed up to axial strains of about 2%. This limit was chosen because we observed
226 that our samples had reached stable post-peak conditions at these strains. Of the 23 total tests we
227 carried out, 5 tests dedicated to microstructural analyses were stopped just after peak stress, at an
228 axial strain of 0.8%. Constant strain rates between 10^{-4} and 10^{-8} s^{-1} were used in order to investigate
229 the strain-rate dependence of the material response (see Table 1 for details on the applied strain rates).

The Young's modulus for all the tests was calculated as the slope of the elastic portion of the stress-strain curve (i.e. the tangent modulus).

In addition to the uniaxial compressive strength tests described above, 14 uniaxial creep tests were performed using the same servo-controlled apparatus. In these experiments, samples were first loaded at a constant strain rate of 10^{-5}/s. After stopping the test for a few seconds, the experiment was continued by controlling for load and, and thus, a constant level of stress (creep conditions) was imposed on the sample (see Heap et al., 2009a-b for details). Because of the variability between samples, the creep stress level was chosen based on the shape of the stress-strain curve beyond the elastic regime. As illustrated in Figure 5, we performed both conventional creep tests and step creep tests, in which the stress level was increased during the experiments by small steps of 1 MPa until sample failure. Specifically, 9 conventional creep and 5 step creep tests were performed. The error of the measured strain rates for both conventional creep and step tests was estimated to be less than 10%.

Figure 5

As previously mentioned, all the tests were performed either under nominally dry or water/oil saturated conditions. For dry conditions, the samples were dried under vacuum at a temperature of 40°C for a minimum of 48h before the tests. Saturated tests (both oil-saturated and water-saturated) were performed after a saturation period of at least two weeks. Tests were performed on samples immersed in the saturating fluid to ensure that samples did not dry out over the course of the experiments (see Heap et al., 2018b for details).

In the discussion, we supplement the above-described laboratory program with some additional tests that have been performed at the purpose to evaluate volumetric evolution during tests.

3.2 Triaxial compression

9 conventional triaxial tests were conducted at room temperature in the servo-controlled triaxial apparatus at ITES, which can reach a maximum confining pressure of 200 MPa. Confining pressure was regulated by a computer-controlled servo motor connected to a pressure transducer with an accuracy of 0.05 MPa. Axial load was applied by a piston and regulated by a second computer-controlled servo motor. Axial displacement was measured with an accuracy of 0.2 μm outside the pressure vessel, with a capacitive transducer mounted on the moving piston, which was servo-controlled to advance at a fixed displacement rate (corresponding to a nominal strain rate of 10^{-5}/s). Details about the set-up and experimental procedure can be found in Baud et al. (2015). Volumetric strain was recorded by monitoring the piston displacement of the confining pressure generator with

an angular encoder. This methodology was previously used for porous limestone by Baud et al. (2009).

The gypsum over-saturated water solution was unsuitable for use in the pore pressure circuit of the triaxial press due to the risk of gypsum precipitation in the pipes. Therefore, to study the influence of water on gypsum under triaxial conditions, we deformed partially saturated samples under undrained conditions, following a procedure recently used by Pijnenburg et al. (2019) on sandstone. Samples were initially saturated with the gypsum-water solution. Then, before the tests, the to-be-tested sample was removed from the solution and allowed to partially de-saturate. The weight of the sample was constantly monitored until 25% of the pore fluid had evaporated. At that moment (with a water saturation of 75%), the sample was mounted into the triaxial press. A specific set of uniaxial tests confirmed the general correspondence of the mechanical data for 100% and 75% water saturation. This is consistent with the study of Schmitt et al. (1994) who did not observe significant changes in the Uniaxial Compression Strength (UCS) of sandstone for water saturation between 100% and 20%. Since our experiments were performed to low levels of volumetric strain (typically <1%), no significant over-pressure could develop in the undrained samples.

3.3 Microstructural analyses

Among the previously described mechanical tests, 12 dedicated tests (5 under uniaxial compression, 4 under creep conditions and 3 under triaxial compression) were performed for microstructural analysis. For these, the experiments were stopped before the complete failure of the sample, slightly after the peak stress. Stress-induced damage in the samples was then analysed on longitudinal thin sections, prepared after saturation with epoxy. Carbon-coated thin sections were investigated with a Cambridge S-360 scanning electron microscope at the University of Turin. Backscattered electron images (BSE) were obtained at an accelerating voltage of 15 kV. Standard petrographic images were also acquired with an Olympus BX4 reflected and transmitted polarized light optical microscope with JENOPTIK ProgResC5 digital colour camera.

4. Results

The experimental dataset consists of 46 mechanical tests (including the 12 dedicated to microstructural analysis): 23 uniaxial loading tests, 14 uniaxial creep tests (9 conventional creep and 5 step creep tests), and 9 conventional triaxial tests. The test conditions and results are reported in the supplementary material and summarised in Table 1, Table 2, and Table 3 respectively.

Table 1

294

295 *4.1 Uniaxial loading mechanical tests*

296 Figure 6a shows some representative stress-strain curves for dry, water-saturated, and oil-saturated
297 samples deformed uniaxially at a strain rate of 10^{-5} s^{-1}. Some variability is typically observed in the
298 uniaxial compressive strength (UCS) of branching selenite gypsum, but water-weakening is clear in
299 Figure 6a. We observed an average reduction of the UCS of about 50%, from 25 MPa under dry
300 conditions to 12 MPa under water-saturated conditions. The Young's modulus was also significantly
301 smaller in the presence of water, with an average reduction of 50%, from 10 GPa for dry samples to
302 5 GPa for wet samples. The strength of the oil-saturated samples was intermediate between these end-
303 members, with mean UCSs of 20 MPa and Young's moduli of 8.5 GPa. In all tests, the peak stress
304 occurred approximately at 0.4% axial strain.

305 We also noted two important differences in the post-peak part of the stress-strain curves between dry
306 and water-saturated samples. Under dry conditions, strain-softening was significantly greater than for
307 water-saturated samples, and was also marked by frequent stress drops with amplitudes ranging from
308 1 to 5 MPa. For water-saturated samples, few to no stress drops were observed and the post peak
309 behaviour was more continuous, with limited softening. The mechanical data for oil-saturated
310 samples were similar to the dry data, showing significant strain-softening characterised by the
311 presence of stress-drops between 1 and 2.5 MPa in amplitude.

312 All UCS values of dry, oil-saturated, and water-saturated tests are summarised in Figure 6b, as a
313 function of porosity. Water saturated samples show a good inverse linear relationship between UCS
314 and porosity, while dry and oil-saturated samples are more scattered. Despite the scatter in the dry
315 data, we observe a clear strength difference between dry and water-saturated samples, with water-
316 saturated samples being weaker. For a given value of porosity, oil-saturated values are lower than dry
317 but higher than water-saturated values.

318 **Figure 6**

319 The effect of strain rate for oil-saturated and water-saturated uniaxial tests is shown in Figure 7 for
320 strain rates between 10^{-4} and 10^{-8} s^{-1}. For oil-saturated samples (Figure 7a), the change in strain rate
321 did not result in significant variations in deformation and failure behaviour: UCS range, softening
322 behaviour and stress-drops in the post peak remained mostly unchanged in all the curves. We assume
323 that similar results could be obtained under dry conditions; we have, however, been unable to verify
324 this due to the difficulty of maintaining stable dry conditions over the experimental timescale (i.e. we
325 cannot control for sample humidity under ambient laboratory conditions).

On the other hand, decreasing strain rate had a significant influence on the results for water-saturated tests (Figure 7b). In particular, the UCS decreased with decreasing strain rate and the post peak behavior changed from strain softening (typical of brittle behavior) to more ductile behavior. A systematic decrease of Young's modulus with decreasing strain rate is also highlighted in Figure 7b.

Figure 7

4.2 Uniaxial creep tests

Table 2 sumarises the results of our uniaxial creep tests (conventional and step tests). The strain-time curves of the conventional creep tests, all performed on water-saturated samples, are shown in Figure 8a. They have the typical features of brittle creep behaviour, as observed in most rock types (see Brantut et al., 2013 for a review). They show an initial phase of decreasing strain rate followed by an inverse trend where the strain rate progressively increases towards failure. There is therefore a minimum strain rate around which the creep strain rate remains quasi-constant for a significant amount of time. We observed significant variability in the recorded minimum strain rates for the same value of applied stress. Figure 8b, showing the values of measured strain rate agains initial porosity, suggests the existence of a direct relationship between these parameters.

Figure 8

Table 2

Because of the variability between samples, we studied the influence of the saturating fluid on time-dependent deformation with step tests. Results, showed in Figure 9 and summarised in Table 2, highlight the clear difference in the strain rate for dry and oil-saturated samples, compared to water-saturated samples. The dry and oil-saturated samples show basically no creep up to relatively high stresses. Close to the short-term strength, a negligible amount of creep was observed before failure. Most of measured strain occurred in the first few seconds of each step (i.e. immediately after the application of the stress). This absence of creep was still observed in the last step before the failure of the sample (i.e. with an applied stress less than 1 MPa lower than the material strength). Water-saturated samples, on the other hand, showed significant creep in all cases with strain rates larger or equal to 5×10^{-9}/s in the first steps. As expected, the strain-rate quickly reached a constant value for the following steps and increased significantly with the applied stress. After a certain amount of strain, the strain rate did not stabilize but accelerated exponentially before the failure of the sample. The maximum strain rate recorded before this last stage of the step tests was 5×10^{-7}/s.

Figure 9

Figure 10 shows the evolution of the strain rate with the applied stress for all our step tests. We found very similar trends (with some offset due to sample variability) for the three water-saturated samples, in agreement with what has been observed in similar tests performed on sandstone (Brantut et al., 2013). Taken together, these data show that the strain rate evolution is the same for all samples, despite the material variability. In all cases, an increase of 5 MPa of the applied stress resulted in an increase of the creep strain of two orders of magnitude. As explained above, no significant creep was observed in oil-saturated and dry samples. For a large interval of stresses, creep occurred at strain rates below the resolution of our system ($\approx 10^{-10}$/s). Then, the maximum strain rate recorded before failure of a dry sample was about 1/4 of the minimum strain rate observed in water-saturated samples.

Figure 10

4.3 Triaxial experiments

Figure 11 shows the mechanical data from the triaxial experiments performed on dry and partially saturated samples. The results are also summarised in Table 3.

Table 3

Experiments on dry samples were performed at confining pressures ranging from 10 to 100 MPa (Figures 11a – black curves). At a confining pressure P_c=10 MPa, the behaviour was typical of brittle deformation with a peak stress followed by strain softening. At all tested confining pressures above 10 MPa, significant strain hardening was observed (Figure11a – black curves). In addition, the stress strain curves were punctured in most cases by small stress-drops, similar to the ones observed in uniaxial compression. Our volumetric strain data revealed dilatancy at all tested pressures up to 100 MPa.

In presence of water (Figure 11a – blue curves), significant weakening is clear at all tested pressures. We noted the absence of softening even at low confining pressures. Between 10 and 80 MPa, we also observed dilatancy (Figure 11b – blue curves). Consistent with our uniaxial data, the presence of water also causes the stress drops to disappear under triaxial conditions.

Figure 11c summarises the results of the triaxial tests in the stress space. As suggested by Brantut et al. (2011), we quantified the yield point using the values of two critical stresses (i.e. the onset dilatancy and the first stress-drop in the dry data). These points are both easy to identify and clear indicators of inelastic behaviour. The values, also reported in Table 3, were found to be similar, except at the highest tested pressure of 100 MPa. The failure envelopes in dry and wet conditions were

388 mostly parallel, indicating that water-weakening was of the same magnitude in the tested pressure
389 range.

390 **Figure 11**

391

392 ## 5. Microstructural observations

393 *5.1 Uniaxial compression*

394 Figure 12 summarises our microstructural observations on samples deformed in uniaxial compression
395 under dry conditions. The interruption of the test just after the peak (with an axial strain of 0.8%)
396 preserved a pattern of coalescing cracks. The main cracks show an aperture of a few tens of μm and
397 sharp borders (Figure 12a-c), occasionally cut through the gypsum grains and are often rimmed by
398 fine-grained material (Figure 12c). Some of these cracks are aligned along a plane with an angle of
399 30° with respect to the applied stress (Figure 12b), while others follow the sub-horizontal layering of
400 the branching selenite (Figure 12d). Since at 0.8% of axial strain the process of failure coalescence is
401 not completed, the cracks show interruptions that correspond to changes in the textural features of the
402 rock (e.g. presence of a layer of finer material – Figure 12a-c). These discontinuities in the failure
403 plane suggest a coalescence "by steps", consistent with the stress-drops in the mechanical data.

404 **Figure 12**

405 In contrast to dry samples, the microstructure of samples deformed under water-saturated conditions
406 (Figure 13) showed the presence of intra-crystalline microcracks, that usually consist of straight
407 parallel fractures that follow the mineral cleavage (Figure 13a-b).

408 Despite this general feature, common to microstructures of all wet samples, some differences may be
409 observed between samples deformed "quickly" (i.e. strain rate = 10^{-5}/s) and "slowly" (i.e. strain rate
410 = 10-7/s or lower or creep conditions). In the former, the majority of cracks are concentrated along a
411 diagonal band of deformation, suggesting a process of coalescence towards a coherent failure plane.
412 In the latter, microcracks are more uniformly distributed in the sample without showing any area of
413 preferential concentration, despite the accumulation of significant amounts of strain (about 2% both
414 in the low-strain rate sample shown in Figures 13b and in the creep sample shown in Figure 13c).
415 This can be more easily understood in Figure 14, which shows the SEM images of the entire thin
416 sections of samples deformed "quickly" (Figures 14a and c) and "slowly" (Figures 14b, d, and e).
417 Figures 14a and c (sample deformed "quickly") show the coalescence of microcracks into the
418 beginnings of a failure surface, while Figures 14b-d-e (sample deformed "slowly") show that the
419 main cracks are oriented subvertically. In addition, slow strain rate and creep samples show the

presence of particular intra-crystalline structures that consist of a series of narrow cracks along the mineral cleavage that, being oriented sub-parallel to the axial applied stress, accommodate the strain by the folding of each separated slice and by the creation of short perpendicular cracks (Figure 13c). The bending of the crystals in creep samples, especially in crystals oriented perpendicular to the applied load, is also evident under the optical microscope. As shown in the Figure 15a-c, some of the larger gypsum crystals in samples tested under creep conditions contain "bands" with a different interference colour than the surrounding portions of the mineral, suggesting a change in the crystallographic orientation. These structures are absent in the initial material (Figure 15d).

All samples deformed under water saturated conditions showed evidence of dissolution. For example, Figure 13d shows an intergranular crack with a 10 to 20 μm aperture and rounded edges that we posit was created by the initial effect of mechanical loading, but enlarged by the dissolution of water.

Figure 13

Figure 14

Figure 15

5.2 Triaxial tests

Consistent with our mechanical data, we only observed a clear, coalesced, macroscopic failure plane in the dry sample deformed at a confining pressure of 10 MPa. As in the uniaxially loaded samples, this failure plane was oriented 30° with respect to the direction of the applied stress (axial). In all other experiments, the final samples did not macroscopically show any failure plane (Figure 16).

Figure 16

Despite this, optical and electron microscope observations showed the pervasive presence of brittle deformation features (i.e. microcracks) as well as evident intra-crystalline plastic structures that deform most of the main crystals in the samples. These structures, shown in Figure 17, consist of bands between a few μm to a few tens of μm thick, oriented perpendicular to the elongation of the crystals (i.e. to the mineral cleavage). In optical microscopy, these bands are highlighted by a change in the birefringence colour (Figure 17a) and in BSE-SEM (Figure 17b) and in SE-SEM (Figure 17c) their boundaries are clearly delineated. Based on these observations, these structures were classified as kink bands (i.e. bands created by two parallel folds with straight limbs and pointed hinges) formed by the folding of the (010) mineral cleavage.

At the tips of the kink bands, intracrystalline cracks that accommodate the plastic deformation created by kinking are commonly observed within the same crystal or in neighbouring ones (Figure 17d).

With the increase of confining pressure, these kink structures appear to be organized in bands (Figure 18).

We observed that also the microstructure of samples deformed under wet conditions was dominated by the kinking of the grains.

Figure 17

Figure 18

6. Discussion

6.1 Water weakening in gypsum

The experimental results show the important influence of water on the mechanical response of gypsum rock over a wide range of conditions. Under uniaxial compression, water-weakening resulted in a decrease in peak strength and Young's modulus of 50% (Figure 6). Similar water-weakening has been reported previously in different gypsum facies (e.g. Yilmaz, 2010). As an illustration, Figure 19a compiles the results of dry and water-saturated uniaxial compression tests on gypsum samples from three different facies: branching selenite gypsum (this study); a massive gypsum facies from the Hafik formation in Sivas basin, Turkey (Yilmaz, 2010); and Volterra gypsum, a very-pure alabastrine gypsum facies with very low porosity and very fine grain-size. To permit direct comparison, we performed a series of uniaxial tests on Volterra gypsum, presented in Annex 5 (supplementary material). Despite the differences in strength (likely related to the differences in microstructural attributes such as texture, porosity, grain size, composition, etc.), an average water-weakening of 52% was obtained in these gypsums and has no clear relationship with porosity.

We note that water-weakening is more significant in tests performed in an open circuit with a continuous flow of fresh water, as observed by Castellanza et al., (2008) These authors reported an exponential weakening of up to 75% over 1 week.

Figure 19

Water-weakening is observed in most rock types, including sandstone (Bell, 1978; 1995; Baud et al., 2000; Duda and Renner, 2013; Tang, 2018; Heap et al., 2019), siltstone (Erguler and Ulusay, 2009; Li et al., 2019), mudstone (Erguler and Ulusay, 2009), granite (Zhuang et al., 2020), basalt (Zhu et al., 2016), andesite (Hashiba et al., 2019), limestone (Ciantia et al., 2015; Baud et al., 2016; Nicolas et al., 2016), and tuff (Erguler and Ulusay 2009; Zhu et al., 2011; Heap et al., 2018a). In Figure 19b, we compare water-weakening in gypsum with existing published data on these rock types. We note that in most cases the authors confirm that uniaxial compression tests were performed on saturated samples after some chemical equilibrium was reached, as in this study. Figure 19b shows that water

weakening in gypsum is not significantly larger than what has been previously observed in other rocks, including sandstones, limestones, tuffs, andesites and basalts.

In sandstone, Baud et al. (2000) used micromechanics to conclude that water-weakening can be explained by a reduction in fracture surface energy and, consequently, of the fracture toughness in the presence of water. In the brittle regime, micromechanical models, such as the pore-emanated crack model (Sammis and Ashby, 1986), predict that the ratio UCS^{wet}/UCS^{dry} is equal to the ratio $K_{IC}{}^{wet}/K_{IC}{}^{dry}$, if $K_{IC}{}^{dry}$ and $K_{IC}{}^{wet}$ are the fracture toughness in nominally dry and water-saturated samples, respectively. It should be noted that this effect would cause a strength reduction in the presence of water even at high strain rates and also for incomplete saturation, as observed in this study. At ambient temperature, Meng et al. (2015) measured a reduction of K_{IC} in a water-saturated gypsum (a marine facies with gypsum content between 60% and 85%) of about 21%. This suggests that water-weakening observed in our gypsum samples can only be partially explained by the reduction of the fracture surface energy.

Other causes commonly suggested to explain water-weakening also involve the dissolution of specific elements of the rock, such as the cement (e.g. depositional bonds among the grains of a calcarenite, Ciantia et al., 2015) or increased solubility of some grains in the rock (e.g. zeolites in volcanic tuffs, Heap et al., 2018a). Our new data suggest a change of failure mechanism in the presence of water, consistent with such processes. Under dry conditions, failure occurs as an unstable stepping mechanism of crack coalescence, as suggested by the episodic stress-drops in the mechanical data (Figure 11a) and by microstructural observations (Figure 12). Under water-saturated conditions, water dissolves material along the grain boundaries and along the surfaces of the mineral cleavage. The observation that cracks propagate along the mineral cleavage (Figure 13) is consistent with the mechanical weakness created by the oriented crystallographic structure of gypsum, that, in the presence of water, is further enhanced by the faster dissolution rate on (010) crystallographic faces (Yu et al., 2016, Fan and Teng, 2007), resulting in a weakening of the grains (see the dense intra-crystalline cracking shown in Figure 13). These processes reduce the overall strength of the rock. This scenario is supported by the disappearance of stress drops in the post-peak stress-strain curves for water-saturated samples (Figure 6a). Indeed, the weakening of grains and intra-grains connections changes the unstable step-wise crack coalescence into a more gradual failure process.

6.2 Time-dependent behaviour

While no significant time-dependent behaviour was observed in samples deformed under dry conditions or saturated with an apolar fluid (i.e. oil), our new data reveal a clear strain rate dependence of strength and significant creep in all samples saturated with gypsum-saturated water. The creep

behaviour of branching selenite gypsum shows the following features: All our creep experiments ended by brittle failure of the samples, meaning that we observed brittle creep in all cases. The brittle creep phenomenology in gypsum was similar to that observed in most other rock types (Brantut et al., 2013). Significantly more strain was recorded before failure in samples deformed at low strain rates and samples with higher porosity (Figure 8 and Table 2).

To delve deeper into the mechanism(s) leading to this time dependent behaviour, we performed additional, targeted experiments on sample of Monferrato gypsum aimed at quantifying porosity change during creep. Porosity was measured before and after creep experiments that were stopped at the onset of the acceleration towards failure (Figure 20a). Because of the significant impact of porosity on the mechanical behaviour of gypsum, and also of sample availability, we focused on end-members: we deformed two samples with high porosity and one with low porosity. The data show that in the three cases significant dilatancy occurred during creep (the difference in porosity was between +0.4% and +1.3%). This is consistent with the previous results of Hoxha et al. (2006), who also reported dilatancy in triaxial creep experiments on samples of a highly pure orogenic gypsum facies from Jura (France), under conditions of high relative humidity. Comparing these results with similar porosity measurements performed on samples deformed at constant strain rates (Figure 20b), we found an overall similar trend in creep and conventional compression tests. Considering the small differences that may be attributed to the initial porosity, higher amounts of accumulated strain correspond to more dilatancy, with the exception of the sample loaded at a strain rate of $10^{-5}\,s^{-1}$, which has significantly higher volumetric increase. Both this dilatancy and the failure mode of the samples suggest that stress-corrosion cracking was the main micromechanism of time-dependent deformation in the branching selenite gypsum.

Figure 20

As discussed by Brantut et al. (2014a-b), an important feature of brittle creep driven by stress corrosion is the fact that the typical increase in strain rate towards failure begins when the inelastic strain for a given creep stress reaches the same value as that of a ("fast") constant strain rate test, as shown for Darley Dale sandstone in Figure 21a. Brantut et al (2014b), however, described a somehow different situation in Purbeck limestone in which they observed significantly more inelastic strain under creep conditions, in particular with low strain rates, than in faster constant strain rate tests (Figure 21b). This was interpreted by the authors to be due to additional mechanisms potentially acting on the top of the dominant action of stress corrosion: plastic flow at microcrack tips (that results in less efficient crack propagation and interaction, producing higher overall strain at failure, since more cracks can be accommodated before coalescence) and pressure solution within the fine-grained

549 matrix (considered as the main mechanism responsible for the compaction observed in the mechanical
550 tests in that study). As shown by Figure 21c, our new data on gypsum suggest a comparable scenario.
551 Indeed, we systematically observe significantly more inelastic strain in all creep tests and tests
552 performed at slow constant strain rates. Figure 21c shows that the difference could in some cases be
553 as high as a factor of 3, suggesting that mechanisms other than stress corrosion must have been active
554 in the material.

555 **Figure 21**

556 As illustrated in Figure 13, the microstructure of the samples that experienced large amounts of
557 inelastic strain (up to 2%) is dominated by microcracking, with a prevalence of intracrystalline cracks
558 along the mineral cleavage (Figure 13). We also observe evidence of plastic structures (Figure 13c
559 and Figure 15).

565 Overall, our microstructural observations, in agreement with the increase of volume identified by the
566 sample porosities reported in Figure 20, do not support pressure solution as a major mechanism of
567 time dependent deformation in our gypsum. Further, the layered crystallographic structure of gypsum
568 allows for the creation of plastic structures (i.e. Figure 13c and Figure 15) with relative ease. Under
569 creep conditions, the lower crack growth rate may result in a more efficient activation of plastic
570 mechanisms and, therefore, predominantly plastic flow. Consequently, shorter cracks and fewer crack
571 interactions are expected resulting in higher overall strain at failure (Brantut et al., 2014b).

572 Brittle creep has been reported in most rock types, under different stress, temperature and
573 environmental conditions - e.g. in sandstone (Baud and Meredith, 1997; Heap et al., 2009a, 2009b;
574 Ngwenya et al., 2001; Tsai et al., 2008), clay (Gasc-Barbier et al., 2004), tuff (Martin et al., 1997),
575 limestone (Brantut et al., 2013), basalt (Heap et al., 2011), and granite (Fujii et al., 1999). Figure 22
576 shows a comparison of our new data on branching selenite gypsum with uniaxial creep data on a
577 saccharoide gypsum (Moiriat et al., 2006), Darley sandstone (Chen et al., 2018), and Purbeck
578 limestone (unpublished data from Brantut et al., 2014b). It should be noted that both datasets on
579 Darley Dale sandstone and Purbeck limestone were obtained in Strasbourg using the same
580 experimental set-up and procedure (see Section 2). For gypsum, the evolution of strain rate with
581 applied stress is well-described by an exponential or power law as observed in other rock types, again
582 supporting stress-corrosion cracking as the main creep micromechanism. We note that the evolution
583 in our data is consistent with Moirat et al. (2006). These authors studied creep in a saccharoide
584 gypsum with textural and mechanical features similar to the facies investigated in this work (i.e. grain
585 size between 0.1 and 1 mm and wet uniaxial strength of 13.7 MPa). Their creep tests were performed,

as in our study, under saturated conditions with gypsum-saturated water, but at significantly lower stresses (not higher than 50% of the UCS). Their creep strain rates were consistently less than 2×10^{-9}/s measured over up to 1 year and, as in our study, their associated microstructural observations revealed microcracks, cracking and fragmentation of grains, which is in overall agreement with our observations. As shown in Figure 22, despite the difference in applied stress and duration of the measurements, the trend suggested by our data is compatible with the order of magnitude of strain rate obtained by Moirat et al., (2016), which was consistently less than 2×10^{-9}/s measured over up to 1 year.

The comparison between gypsum and other rocks in Figure 22 shows that the creep strain rate in gypsum was significantly less sensitive to the applied stress than in Darley Dale sandstone and Purbeck limestone, as confirmed by the exponent's constant (about 14 in gypsum and 30 in the other rocks). This can be interpreted either as a lower stress corrosion index for gypsum or due to the complex influence of several mechanisms, though the latter is unlikely based on our observations. More systematic creep experiments under confinement would be needed to provide definitive conclusions and this should be a target for future studies. From a geotechnical point of view, the data presented in Figure 22 suggest that the long-term evolution of gypsum's mechanical behaviour could be easier to predict than in other rock types. This is because, according to data in Figure 10 and in Figure 22, the strain rates observed in gypsum are less sensitive to the applied stress.

Figure 22

6.3 Impact of effective pressure

Our triaxial data on branching selenite gypsum show a classical increase of the strength with confining pressure under both dry and wet conditions without any major macroscopic change in failure mechanism between confining pressures of 20 and 100 MPa (Figure 16). The water weakening under triaxial conditions was consistent with our uniaxial data, analysed in section 6.1. Focusing on the dry data, we note the very strong similarities between our mechanical data and those from the earlier study of Brantut et al. (2011) on Volterra gypsum. For both rocks, clear strain softening was only observed up to a confinement of 10 MPa and associated with a major shear band. At higher pressures, deformation was localized along multiple shear bands (see Figure 18) and small stress drops of comparable amplitudes were observed. In addition, a similarity of microstructures was observed between our material and Brantut et al. (2011)'s: in both studies, deformation appears to be driven by intracrystalline plastic mechanisms that result in kink bands. As suggested by Brantut et al. (2011), these structures are consistent with the hardening in the mechanical data because of the finite strain that can be accommodated by a single grain. Once the maximum folding was reached, the

energy required to start to kink a new grain was lower than the energy needed to bring the grain to failure.

In contrast to Brantut et al. (2011)'s study, we could measure the volumetric strain during our experiments on branching selenite gypsum. Dilatancy was observed even at the highest tested pressures, which suggests that mostly dilatant structures developed in our samples. This is however consistent with the kink deformation observed in microstructures. Indeed, as shown in Figure 17d, the creation of kink bands is often associated with the opening of intracrystalline cracks at the tip of the bands. Since this is similar to the observed post-deformation microstructures in Volterra gypsum (Brantut et al., 2011), we can speculate that this was also the case in that rock. This macroscopic volume increase does not however rule out the possibility that local compaction occurred in some parts of our samples, particularly at high effective pressures, as it has recently been shown in carbonates using X-ray computed tomography and digital volume correlation by Baud et al. (2021).

Data on triaxially deformed gypsum are scarce and it was therefore interesting to compare our new results with existing data on Volterra gypsum. However, due to the strong impact of sample size on strength (Paterson and Wong, 2005, Bozorgzadeh et al, 2017, Gao et al., 2018), we were unable to perform this comparison using the results of Brantut et al. (2011), despite the similarities with our data. We instead present in Figure 23 a comparison of the dry failure envelopes of branching selenite gypsum (from this study) and of Volterra gypsum based on the study of Olgaard et al. (1995), who used a comparable sample size. Two important observations can be made. First, Volterra gypsum is significantly stronger than branching selenite gypsum, in agreement with our uniaxial data (see supplementary material S1). This large difference is most certainly due to a combination of factors: the very low porosity and smaller grain size of Volterra (about 1 mm in branching selenite and 100 µm in Volterra gypsum) and the presence of secondary minerals such as clay in branching selenite gypsum (compared to 99% gypsum in Volterra). Secondly, the shape of the failure envelope of branching selenite gypsum suggests that beyond an effective pressure of 150 MPa, the behavior may switch to a cap-like envelope associated with shear-enhanced compaction, as observed in other tight rocks (e.g. Solnhofen limestone Baud et al., 2000 or basalts Zhu et al., 2016). To our knowledge, this switch in gypsum behaviour has not been observed to date. Further tests, under high confining pressures, are required to confirm this hypothesis.

Figure 23

6.4 Implications for quarry exploitation

As confirmed by Figure 19a, a water weakening of 50% in strength is observed in most gypsum facies, despite differences in dry strength.

This may have impact on several societally relevant fields, the most obvious being the reduction of geological risks underground. There are many examples of subsurface rock bodies in which water circulates. The impact of water on the mechanical performance of the rock is therefore relevant, necessitating dedicated stability assessments of long-term underground excavations (e.g. civil and mining tunnels, caverns, etc.). The decrease of gypsum strength, both under uniaxial and triaxial loading conditions, and the enhancement of creep deformation in water described in this paper may significantly affect the general stability of the voids.

The water-related weakening of gypsum, particularly if associated with underground tunnels, may also enhance sinkhole and surface subsidence risk scenarios.

In recent years, the behaviour of gypsum and other salt minerals has raised the interest of the scientific community due to the possibility of using salt caverns for energy storage including Underground Gas Storage (UGS) and Compressed Air Energy Storage (CAES). Salt caverns have also been identified as key elements for the bulk storage of hydrogen, nowadays considered as the best decarbonization option for long-term seasonal energy storage. However, these 'new' applications are not yet cost competitive, in part because of the gaps in knowledge about the mechanical response of evaporite rocks.

In this context, the outcomes of this study provide new fundamental elements that may inform our understanding of the feasibility of energy storage strategies.

7. Conclusions

In this work, we study the impact of water on the strength and rheology of gypsum rock. Our main results may be summarised as follows:

1. Under uniaxial compression, the strength of water-saturated branching selenite gypsum is about half of its value under nominally dry conditions. Moreover, water also induces certain changes in the mechanical behaviour (e.g. disappearance of stress drops, limited strain softening). Our microstructural observations suggest that water weakening is due to the combined effect of the reduction of the fracture surface energy and dissolution along the surfaces of the mineral cleavage, weakening the crystals' strength.
2. Under uniaxial compression, significant time dependent behaviour is observed in the presence of water but not in dry or oil-saturated samples. The UCS of gypsum decreases with decreasing strain rate. Moreover, brittle creep is observed at stresses beyond the elastic

regime. Creep in gypsum is strongly influenced by sample variability but our data show that the initial porosity of the material has a major impact on creep strain rates. The main attributes of brittle creep in gypsum are broadly similar to those of other rock types. Dilatancy and stress-induced microcracking point to stress corrosion as the main mechanism of time dependent deformation in gypsum. At low strain rates however, more strain is observed suggesting the action of other mechanisms.

3. Deformation of gypsum under triaxial compression is driven by kinking of the gypsum grains and is dilatant up to high confining pressures (i.e. 100 MPa). The water-weakening quantified at high pressures is similar to our observations under uniaxial compression. Comparison of our new data with published results on Volterra gypsum highlights the inverse relationship between porosity and triaxial yield point in gypsum. Our triaxial data suggest that shear-enhanced compaction, which was not observed at the conditions of our experiments, could possibly develop in branching selenite gypsum at confining pressures beyond 150 MPa.

Acknowledgments

The authors would like to thank the Private Company that made available the cores of branching selenite for this experimental investigation. We also thank Alex Schubnel for providing Volterra gypsum for additional experimental tests and comparison. Sincere thanks are also due to Mike Heap for the useful discussions that helped to improve the quality of this research and to Simona Cavagna for the fundamental help in SEM investigation.

References

Auvray, C., Homand, F., Sorgi, C., 2004. The aging of gypsum in underground mines. Eng. Geol. 74, 183–196. https://doi.org/10.1016/j.enggeo.2004.03.008

Baud, P., Meredith, P.G., 1997. Damage accumulation during triaxial creep of Darley Dale sandstone from pore volumometry and acoustic emission. Int. J. Rock Mech. Min. Sci. 34, 24.e1-24.e10. https://doi.org/10.1016/S1365-1609(97)00060-9

Baud, P., Zhu, W., Wong, T., 2000. Failure mode and weakening effect of water on sandstone. J. Geophys. Res. Solid Earth 105, 16371–16389. https://doi.org/10.1029/2000JB900087

Baud, P., Vinciguerra, S., David, C., Cavallo, A., Walker, E., Reuschlé, T., 2009. Compaction and Failure in High Porosity Carbonates: Mechanical Data and Microstructural Observations. Pure Appl. Geophys. 166, 869–898. https://doi.org/10.1007/s00024-009-0493-2

Baud, P., Reuschlé, T., Ji, Y., Cheung, C.S.N., Wong, T., 2015. Mechanical compaction and strain localization in Bleurswiller sandstone. J. Geophys. Res. Solid Earth 120, 6501–6522. https://doi.org/10.1002/2015JB012192

Baud, P., Rolland, A., Heap, M., Xu, T., Nicolé, M., Ferrand, T., Reuschlé, T., Toussaint, R., Conil, N., 2016. Impact of stylolites on the mechanical strength of limestone. Tectonophysics 690, 4–20. https://doi.org/10.1016/j.tecto.2016.03.004

Baud, P., Hall, S., Heap, M.J., Ji, Y., Wong, T.-F., 2021. The Brittle-Ductile Transition in Porous Limestone: Failure Mode, Constitutive Modeling of Inelastic Deformation and Strain

721 Localization. Journal of Geophysical Research: Solid Earth 126.
722 https://doi.org/10.1029/2020JB021602
723 Bell, F.G., 1978. The physical and mechanical properties of the fellsandstones, Northumberland,
724 England. Eng. Geol. 12, 1–29.
725 Bell, F.G., 1995. Laboratory testing of rocks. In: Bell, F.G. (Ed.), Engineering in Rock, pp. 151–
726 169.
727 Bertotti, G., Mosca, P. 2009. Late Orogenic Vertical Movements within the Arc of the SW Alps and
728 Ligurian Alps. Tectonophysics 475(1), pp 117-127.
729 https://doi:10.1016/J.TECTO.2008.08.016.
730 Bozorgzadeh, N., Yanagimura, Y., Harrison, J.P. 2017. Effect of Small Numbers of Test Results on
731 Accuracy of Hoek–Brown Strength Parameter Estimations: A Statistical Simulation
732 Study. Rock Mech Rock Eng 50, 3293–3305. https://doi.org/10.1007/s00603-017-1352-6
733 Bonetto, S., Fiorucci, A., Fornaro, M., Vigna, B., 2008. Subsidence hazard connected to
734 quarrying activities in a karst area:a case of the Moncalvo sinkhole event (Piedmont, NW
735 Italy). Estonian Journal of Earth Science 57, 125-134
736 Brantut, N., Schubnel, A., Guéguen, Y., 2011. Damage and rupture dynamics at the brittle-ductile
737 transition: The case of gypsum. J. Geophys. Res. Solid Earth 116.
738 https://doi.org/10.1029/2010JB007675
739 Brantut, N., Heap, M.J., Meredith, P.G., Baud, P., 2013. Time-dependent cracking and brittle creep
740 in crustal rocks: A review. J. Struct. Geol. 52, 17–43.
741 https://doi.org/10.1016/j.jsg.2013.03.007
742 Brantut, N., Heap, M.J., Baud, P., Meredith, P.G., 2014a. Rate- and strain-dependent brittle
743 deformation of rocks. J. Geophys. Res. Solid Earth 119, 1818–1836.
744 https://doi.org/10.1002/2013JB010448
745 Brantut, N., Heap, M.J., Baud, P., Meredith, P.G., 2014b. Mechanisms of time-dependent
746 deformation in porous limestone. J. Geophys. Res. Solid Earth 119, 5444–5463.
747 https://doi.org/10.1002/2014JB011186
748 Caselle, C., Bonetto, S., Colombero, C., Comina, C., 2019a. Mechanical properties of
749 microcrystalline branching selenite gypsum samples and influence of constituting factors.
750 Journal of Rock Mechanics and Geotechnical Engineering 11, 228–241.
751 https://doi.org/10.1016/j.jrmge.2018.09.003
752 Caselle, C., Bonetto, S., Vagnon, F., Costanzo, D., 2019b. Dependence of macro mechanical
753 behaviour of gypsum on micro-scale grain-size distribution. Géotechnique Lett. 1–9.
754 https://doi.org/10.1680/jgele.18.00206
755 Caselle, C., Bonetto, S., Vagnon, F., Ferrero, A.M., Cardu, M., Costanzo, D., 2020a. Micro-scale
756 mechanisms controlling the deformation and failure of gypsum. Presented at the ISRM
757 International Symposium - EUROCK 2020.
758 Caselle, C., Bonetto, S.M.R., Costanzo, D., 2020b. Crack coalescence and strain accommodation in
759 gypsum rock. Frat. Ed Integrità Strutt. 14, 247–255. https://doi.org/10.3221/IGF-ESIS.52.19
760 Caselle, C., Umili, G., Bonetto, S., Costanzo, D., Ferrero, A.M., 2020c. Evolution of Local Strains
761 Under Uniaxial Compression in an Anisotropic Gypsum Sample. Lecture Notes in Civil
762 Engineering 40, 454–461. https://doi.org/10.1007/978-3-030-21359-6_48
763 Caselle, C., Pastero, L., Cavagna, S., Bonetto, S. 2022. Preliminary Mineralogical Characterization
764 of Branching Selenite Gypsum: New Insights for the Paleoenvironmental Reconstruction
765 and Mechanical Characterization, Minerals 2022, 12, 378.
766 https://doi.org/10.3390/min12030378
767 Castellanza, R., Gerolymatou, E., Nova, R., 2008. An Attempt to Predict the Failure Time of
768 Abandoned Mine Pillars. Rock Mech. Rock Eng. 41, 377–401.
769 https://doi.org/10.1007/s00603-007-0142-y

Castellanza, R., Nova, R., Orlandi, G., 2010. Evaluation and remediation of an abandoned gypsum mine. J. Geotech. Geoenvironmental Eng. 136, 629–639. https://doi.org/10.1061/(ASCE)GT.1943-5606.0000249

Chen, C., Xu, T., Heap, M.J., Baud, P., 2018. Influence of unloading and loading stress cycles on the creep behavior of Darley Dale Sandstone. Int. J. Rock Mech. Min. Sci. 112, 55–63. https://doi.org/10.1016/j.ijrmms.2018.09.002

Ciantia, M.O., Castellanza, R., di Prisco, C., 2015. Experimental Study on the Water-Induced Weakening of Calcarenites. Rock Mech. Rock Eng. 48, 441–461. https://doi.org/10.1007/s00603-014-0603-z

Cipriani, M., Dominici, R., Costanzo, A., D'Antonio, M., Guido, A. 2021 A Messinian Gypsum Deposit in the Ionian Forearc Basin (Benestare, Calabria, Southern Italy): Origin and Paleoenvironmental Indications. Minerals, 11, 1305, doi:10.3390/min11121305.

Clari, P., Dela Pierre, F., Novaretti, A., Timpanelli, M., 1995. Late Oligocene-Miocene sedimentary evolution of the critical Alps/Apennines junction: the Monferrato area. Northwestern Italy. Terra Nova 7, 144–152. https://doi.org/10.1111/j.1365-3121.1995.tb00683.x

Craker, W.E., Schiller, K.K., 1962. Plastic deformation of gypsum. Nature 193, 672–673. https://doi.org/10.1038/193672a0

Cristallini, E.O, Ramos V.A. 2000. Thick-skinned and thin-skinned thrusting in the La Ramada fold and thrust belt: Crustal evolution of the High Andes of San Juan, Argentina (32°SL). Tectonophysics 317(3–4), 205-235. https://doi.org/10.1016/S0040-1951(99)00276-0

Croizé, D., Renard, F. Gratier, J.-P. 2013. Compaction and Porosity Reduction in Carbonates: A Review of Observations, Theory, and Experiments. Advances in Geophysics, Academic Press Inc. https://doi.org/10.1016/B978-0-12-380940-7.00003-2

de Meer, S., Spiers, C.J., 1995. Creep of wet gypsum aggregates under hydrostatic loading conditions. Tectonophysics, Influence of Fluids on Deformation Processes in Rocks 245, 171–183. https://doi.org/10.1016/0040-1951(94)00233-Y

de Meer, S., Spiers, C.J., 1997. Uniaxial compaction creep of wet gypsum aggregates. J. Geophys. Res. Solid Earth 102, 875–891. https://doi.org/10.1029/96JB02481

de Meer, S., Spiers, C.J., 1999. Influence of pore-fluid salinity on pressure solution creep in gypsum. Tectonophysics 308, 311–330.

Dela Pierre, F., Bernardi, E., Cavagna, S., Clari, P., Gennari, R., Irace, A., Lozar, F., Lugli, S., Manzi, V., Natalicchio, M., Roveri, M., Violanti, D., 2011. The record of the Messinian salinity crisis in the Tertiary Piedmont Basin (NW Italy): The Alba section revisited. Palaeogeogr. Palaeoclimatol. Palaeoecol. 310, 238–255. https://doi.org/10.1016/j.palaeo.2011.07.017

Dela Pierre, F., Natalicchio, M., Lozar, F., Bonetto, S., Carnevale, G., Cavagna, S., Colombero, S., Sabino, M., Violanti, D., 2016. The northernmost record of the Messinian salinity crisis (Piedmont basin, Italy). Geol.F.Trips 8, 58.

Delage, P., Schroeder, C., Cui, Y.J., 1996. Subsidence and capillary effects in chalks. Eurock'96. Balkema, Rotterdam, 1291– 1298.

Duda, M., Renner, J., 2013. The weakening effect of water on the brittle failure strength of sandstone. Geophys. J. Int. 192, 1091–1108. https://doi.org/10.1093/gji/ggs090

EN-ISO 17892-3:2015. Geotechnical investigation and testing — Laboratory testing of soil — Part 3: Determination of particle density.

Erguler, Z.A., Ulusay, R., 2009. Water-induced variations in mechanical properties of clay-bearing rocks. Int. J. Rock Mech. Min. Sci. 46, 355–370.

Fan, C., Teng, H.H., 2007. Surface behavior of gypsum during dissolution. Chem. Geol. 245, 242–253. https://doi.org/10.1016/j.chemgeo.2007.08.007

Fujii, Y., Kiyama, T., Ishijima, Y., Kodama, J., 1999. Circumferential strain behavior during creep tests of brittle rocks. Int. J. Rock Mech. Min. Sci. 36, 323–337.

Gao, K., Harrison, J.P. 2018. Multivariate distribution model for stress variability characterization. International Journal of Rock Mechanics and Mining Sciences 102, 144-154

Gasc-Barbier, M., Chanchole, S., Bérest, P., 2004. Creep behavior of Bure clayey rock. Appl. Clay Sci., Clays in Natural and Engineered Barriers for Radioactive Waste Confinement 26, 449–458. https://doi.org/10.1016/j.clay.2003.12.030

Geremia, D. David, C., Descamps, F., Menéndez, B., Barnes, C., Vandycke, S., Dautriat, J., Esteban, L., Sarout, J. 2021. Water-induced damage in microporous carbonate rock by low-pressure injection test. Rock Mechanics and Rock Engineering, 54, 5185-5206.

Hashiba, K., Fukui, K., Kataoka, M., 2019. Effects of water saturation on the strength and loading-rate dependence of andesite. Int. J. Rock Mech. Min. Sci. 117, 142–149. https://doi.org/10.1016/j.ijrmms.2019.03.023

Heap, M.J., Baud, P., Meredith, P.G., 2009a. Influence of temperature on brittle creep in sandstones. Geophys. Res. Lett. 36. https://doi.org/10.1029/2009GL039373

Heap, M.J., Baud, P., Meredith, P.G., Bell, A.F., Main, I.G., 2009b. Time-dependent brittle creep in Darley Dale sandstone. J. Geophys. Res. Solid Earth 114. https://doi.org/10.1029/2008JB006212

Heap, M.J., Baud, P., Meredith, P.G., Vinciguerra, S., Bell, A.F., Main, I.G., 2011. Brittle creep in basalt and its application to time-dependent volcano deformation. Earth Planet. Sci. Lett. 307, 71–82. https://doi.org/10.1016/j.epsl.2011.04.035

Heap, M.J., Lavallée, Y., Petrakova, L., Baud, P., Reuschlé, T., Varley, N.R., Dingwell, D.B., 2014. Microstructural controls on the physical and mechanical properties of edifice-forming andesites at Volcán de Colima, Mexico. J. Geophys. Res. Solid Earth 119, 2925–2963. https://doi.org/10.1002/2013JB010521

Heap, M.J., Kushnir, A.R.L., Gilg, H.A., Wadsworth, F.B., Reuschlé, T., Baud, P., 2017. Microstructural and petrophysical properties of the Permo-Triassic sandstones (Buntsandstein) from the Soultz-sous-Forêts geothermal site (France). Geotherm. Energy 5, 26. https://doi.org/10.1186/s40517-017-0085-9

Heap, M.J., Farquharson, J.I., Kushnir, A.R.L., Lavallée, Y., Baud, P., Gilg, H.A., Reuschlé, T., 2018a. The influence of water on the strength of Neapolitan Yellow Tuff, the most widely used building stone in Naples (Italy). Bull. Volcanol. 80, 51. https://doi.org/10.1007/s00445-018-1225-1

Heap, M.J., Thierry R., Kushnir A.R.L., Baud P. 2018b. The influence of hydrothermal brine on the short-term strength and elastic modulus of sandstones from exploration well EPS-1 at Soultz-sous-Forêts (France). Geothermal Energy 6(29). https://doi.org/10.1186/s40517-018-0116-1

Heap, M.J., Villeneuve, M., Kushnir, A.R.L., Farquharson, J.I., Baud, P., Reuschlé, T., 2019. Rock mass strength and elastic modulus of the Buntsandstein: An important lithostratigraphic unit for geothermal exploitation in the Upper Rhine Graben. Geothermics 77, 236–256. https://doi.org/10.1016/j.geothermics.2018.10.003

Heard H.C., Rubey W.W. 1996. Tectonic Implications of Gypsum Dehydration. GSA Bulletin 77 (7): 741–760. https://doi.org/10.1130/0016-7606(1966)77[741:TIOGD]2.0.CO;2

Hoxha, D., Giraud, A., Homand, F., 2005. Modelling long-term behaviour of a natural gypsum rock. Mech. Mater. 37, 1223–1241. https://doi.org/10.1016/j.mechmat.2005.06.002

Hoxha, D., Homand, F., Auvray, C., 2006. Deformation of natural gypsum rock: Mechanisms and questions. Eng. Geol. 86, 1–17. https://doi.org/10.1016/j.enggeo.2006.04.002

Li, B., Liu, J., Bian, K., Ai, F., Hu, X., Chen, M., Liu, Z., 2019. Experimental study on the mechanical properties weakening mechanism of siltstone with different water content. Arab J Geosci 12, 656. https://doi.org/10.1007/s12517-019-4852-

Liang, W., Yang, X., Gao, H., Zhang, C., Zhao, Y., Dusseault, M.B., 2012. Experimental study of mechanical properties of gypsum soaked in brine. Int. J. Rock Mech. Min. Sci. 53, 142–150. https://doi.org/10.1016/j.ijrmms.2012.05.015

Lugli, S., Manzi, V., Roveri, M., Schreiber, C.B., 2010. The Primary Lower Gypsum in the Mediterranean: A new facies interpretation for the first stage of the Messinian salinity crisis. Palaeogeogr. Palaeoclimatol. Palaeoecol. 297, 83–99. https://doi.org/10.1016/j.palaeo.2010.07.017

Martin, R.J., Noel, J.S., Boyd, P.J., Price, R.H., 1997. Creep and static fatigue of welded tuff from Yucca Mountain, Nevada. Int. J. Rock Mech. Min. Sci. 34, 190.e1-190.e17. https://doi.org/10.1016/S1365-1609(97)00179-2

Meng, T., Hu, Y., Fang, R., Kok, J., Fu, Q., Feng, G., 2015. Study of fracture toughness and weakening mechanisms in gypsum interlayers in corrosive environments. J. Nat. Gas Sci. Eng. 26, 356–366. https://doi.org/10.1016/j.jngse.2015.06.027

Meng, T., Xiangxi, M., Donghua, Z., Hu, Y., 2018. Using micro-computed tomography and scanning electron microscopy to assess the morphological evolution and fractal dimension of a salt-gypsum rock subjected to a coupled thermal-hydrological-chemical environment. Mar. Pet. Geol. 98, 316–334. https://doi.org/10.1016/j.marpetgeo.2018.08.024

Meng, F., Li, X., Baud, P., Wong, T.-F. 2020. Effective stress law for the permeability and pore volume change of clayey sandstones, Journal of Geophysical Research: Solid Earth, 125(8), https://doi.org/e2020JB019765.

Moiriat, D., Potherat, P., Massieu, E., Durville, J.-L., 2006. Données expérimentales sur le fluage du gypse saccharoïde en condition saturée. Rev. Fr. Géotechnique 3–10. https://doi.org/10.1051/geotech/2006115003

Natalicchio, M., Pellegrino, L., Clari, P., Pastero, L., Dela Pierre, F. 2021. Gypsum Lithofacies and Stratigraphic Architecture of a Messinian Marginal Basin (Piedmont Basin, NW Italy). Sedimentary Geology, 425, 106009, doi:10.1016/j.sedgeo.2021.106009.

Nicolas, A., Fortin, J., Regnet, J.B., Dimanov, A., Guéguen, Y., 2016. Brittle and semi-brittle behaviours of a carbonate rock: influence of water and temperature. Geophys. J. Int. 206, 438–456. https://doi.org/10.1093/gji/ggw154

Ngwenya, B.T., Main, I.G., Elphick, S.C., Crawford, B.R., Smart, B.G.D., 2001. A constitutive law for low-temperature creep of water-saturated sandstones. J. Geophys. Res. Solid Earth 106, 21811–21826. https://doi.org/10.1029/2001JB000403

Noël, C., Baud, P., Violay, M. 2021. Effect of water on sandstone's fracture toughness and frictional parameters: Brittle strength constraints. International Journal of Rock Mechanics and Mining Sciences 147, 104916. https://doi.org/10.1016/j.ijrmms.2021.104916

Olgaard, D.L., Ko, S., Wong, T., 1995. Deformation and pore pressure in dehydrating gypsum under transiently drained conditions. Tectonophysics 245, 237–248.

Papadopoulos, Z., Kolaiti, E., Mourtzas, N., 1994. The effect of crystal size on geotechnical properties of Neogene gypsum in Crete. Q. J. Eng. Geol. 27, 267–273.

Paterson, M.S., Wong, T., 2005. Experimental Rock Deformation - The Brittle Field, 2nd ed. Springer-Verlag, Berlin Heidelberg. https://doi.org/10.1007/b137431

Piana, F., Polino, R., 1995. Tertiary structural relationships between Alps and Apennines: the critical Torino Hill and Monferrato area. Northwestern Italy. Terra Nova 7, 138–143. https://doi.org/10.1111/j.1365-3121.1995.tb00682.x

Pijnenburg, R.P.J., Verberne, B.A., Hangx, S.J.T., Spiers, C.J., 2019. Intergranular Clay Films Control Inelastic Deformation in the Groningen Gas Reservoir: Evidence From Split-Cylinder Deformation Tests. J. Geophys. Res. Solid Earth 124, 12679–12702. https://doi.org/10.1029/2019JB018702

Ramon, A., Caselle, C., Bonetto, S.M.R., Costanzo, D., Alonso, E.E., 2021. Effect of Microstructure and Relative Humidity on Strength and Creep of Gypsum. Rock Mech. Rock Eng. https://doi.org/10.1007/s00603-021-02510-2

Risnes, R., Madland, M.V., Hole, M., Kwabiah, N.K. 2005. Water-weakening of chalk – Mechanical effect of water-glycol mixture, Journal of Petroleum Science and Engineering 48, 21-36.

Rossi, M., Mosca, P., Polino, R., Rogledi, S., Biffi, U. 2009. New outcrop and subsurface data in the Tertiary Piedmont Basin (NW-Italy): unconformity-bounded stratigraphic units and their relationships with basin-modification phases. Rivista Italiana di Paleontologia e Stratigrafia 115, https://doi.org/10.13130/2039-4942/6386.

Røyne, A., Bisschop, J., Dysthe, D.K. 2011. Experimental investigation of surface energy and subcritical crackgrowth in calcite, J. Geophys. Res.,116, B04204, https://doi.org/10.1029/2010JB008033

Sadeghiamirshahidi, M., Vitton, S.J., 2019. Laboratory Study of Gypsum Dissolution Rates for an Abandoned Underground Mine. Rock Mech. Rock Eng. 52, 2053–2066. https://doi.org/10.1007/s00603-018-1696-6

Sammis, C. G., and Ashby, M. F., 1986. The failure of brittle porous solids under compressive stress states, Acta metall, 34, 511–526.

Schmitt, L., Forsans, T., Santarelli, F.J., 1994. Shale testing and capillary phenomena. Int. J. Rock Mech. Min. Sci. Geomech. Abstr. 31, 411–427. https://doi.org/10.1016/0148-9062(94)90145-7

Tang, S., 2018. The effects of water on the strength of black sandstone in a brittle regime. Eng. Geol. 239, 167–178. https://doi.org/10.1016/j.enggeo.2018.03.025

Toussaint, R., Aharonov, E., Koehn, D., Gratier, J.-P., Ebner, M., Baud, P., Rolland, A., and Renard F. (2018), Stylolites: A review. J. Struct. Geol., 114, 163-195.

Tsai, L.S., Hsieh, Y.M., Weng, M.C., Huang, T.H., Jeng, F.S., 2008. Time-dependent deformation behaviors of weak sandstones. Int. J. Rock Mech. Min. Sci. 45, 144–154. https://doi.org/10.1016/j.ijrmms.2007.04.008

Wang, J.-A., Shang, X.C., Ma, H.T., 2008. Investigation of catastrophic ground collapse in Xingtai gypsum mines in China. Int. J. Rock Mech. Min. Sci. 45, 1480–1499. https://doi.org/10.1016/j.ijrmms.2008.02.012

Yilmaz, I., 2007. Differences in the geotechnical properties of two types of gypsum: alabastrine and porphyritic. Bull. Eng. Geol. Environ. 66, 187–195. https://doi.org/10.1007/s10064-006-0055-0

Yilmaz, I., 2010. Influence of water content on the strength and deformability of gypsum. Int. J. Rock Mech. Min. Sci. 47, 342–347. https://doi.org/10.1016/j.ijrmms.2009.09.002

Yu, W.D., Liang, W.G., Li, Y.R., Yu, Y.M., 2016. The meso-mechanism study of gypsum rock weakening in brine solutions. Bull. Eng. Geol. Environ. 75, 359–367. https://doi.org/10.1007/s10064-015-0725-x

Zhu, W., Baud, P., Vinciguerra, S., Wong, T.-F., 2011. Micromechanics of brittle faulting and cataclastic flow in Alban Hills tuff. Journal of Geophysical Research: Solid Earth 116. https://doi.org/10.1029/2010JB008046

Zhu, W., Baud, P., Vinciguerra, S., Wong, T., 2016. Micromechanics of brittle faulting and cataclastic flow in Mount Etna basalt. Journal of Geophysical Research: Solid Earth 121, 4268–4289. https://doi.org/10.1002/2016JB012826

Zhu, C., Xu, X., Liu, W., Xiong, F., Lin, Y., Cao, C., Liu, X., 2019. Softening Damage Analysis of Gypsum Rock With Water Immersion Time Based on Laboratory Experiment. IEEE Access 7, 125575–125585. https://doi.org/10.1109/ACCESS.2019.2939013

Zhuang, L., Kim, K.Y., Diaz, M., Yeom, S., 2020. Evaluation of water saturation effect on mechanical properties and hydraulic fracturing behavior of granite. International Journal of Rock Mechanics and Mining Sciences 130, 104321. https://doi.org/10.1016/j.ijrmms.2020.104321

Zucali, M., Barberini, V., Chateigner, D., Ouladdiaf, B., Lutterotti, L., 2010. Brittle plus plastic deformation of gypsum aggregates experimentally deformed in torsion to high strains: Quantitative microstructural and texture analysis from optical and diffraction data. Geol. Soc. Lond. Spec. Publ. 332, 79-98. doi:10.1144/SP332.6. https://doi.org/10.1144/SP332.6

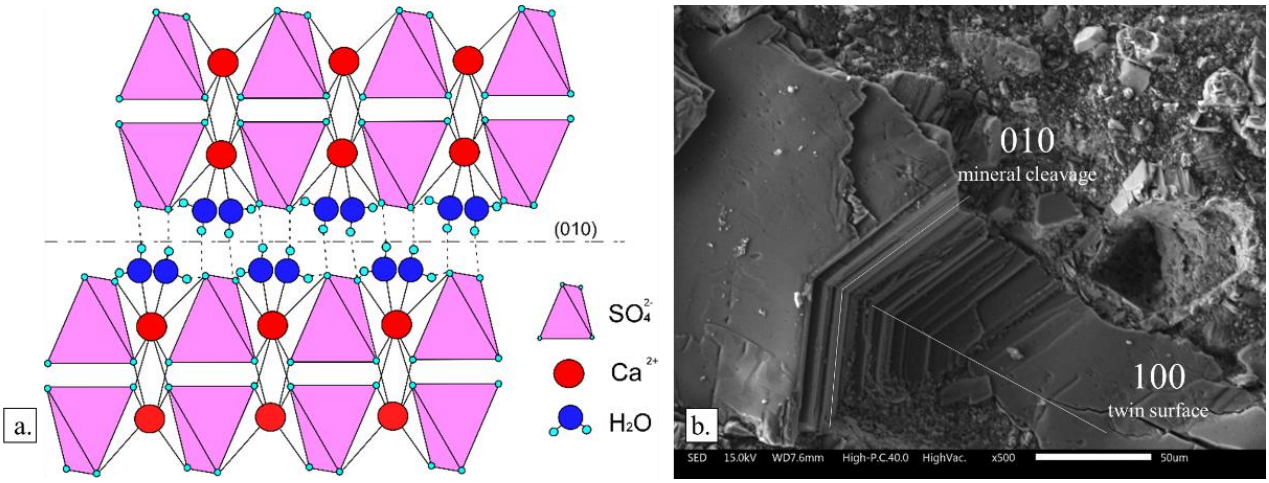

973
974

975 Figure 1. (a) Crystallographic structure of gypsum. (b) Selenite crystal, with the perfect mineral
976 cleavage on the (010) crystallographic direction and the contact twin on the (100) crystallographic
977 plane.

978

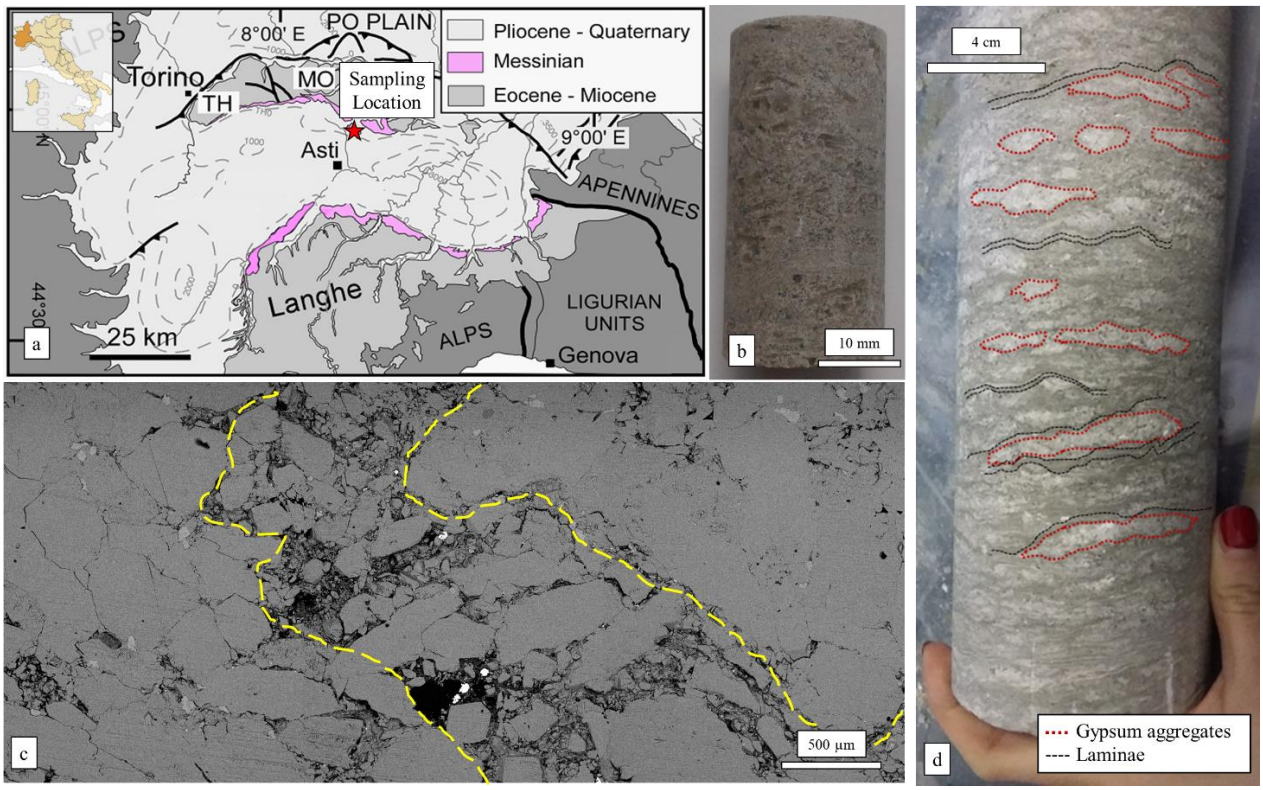

Figure 2. (a) Map of the test area, showing the areal distribution of Messinian gypsum deposits in Piedmont and the geographical position of the sampling site (red star); TH = Torino Hill, MO = Monferrato. (b) 40mm by 20mm sample of branching selenite gypsum, before deformation. (c) BSE-SEM microstructure of the branching selenite gypsum, showing the main features of this facies: the yellow dashed lines show the boundary between the nodules of gypsum crystals (on the right and on the left) and the finer material (in the middle). (d) Initial borehole core, before resampling. Examples of gypsum aggregates and laminae are highlighted using red and black dotted lines respectively.

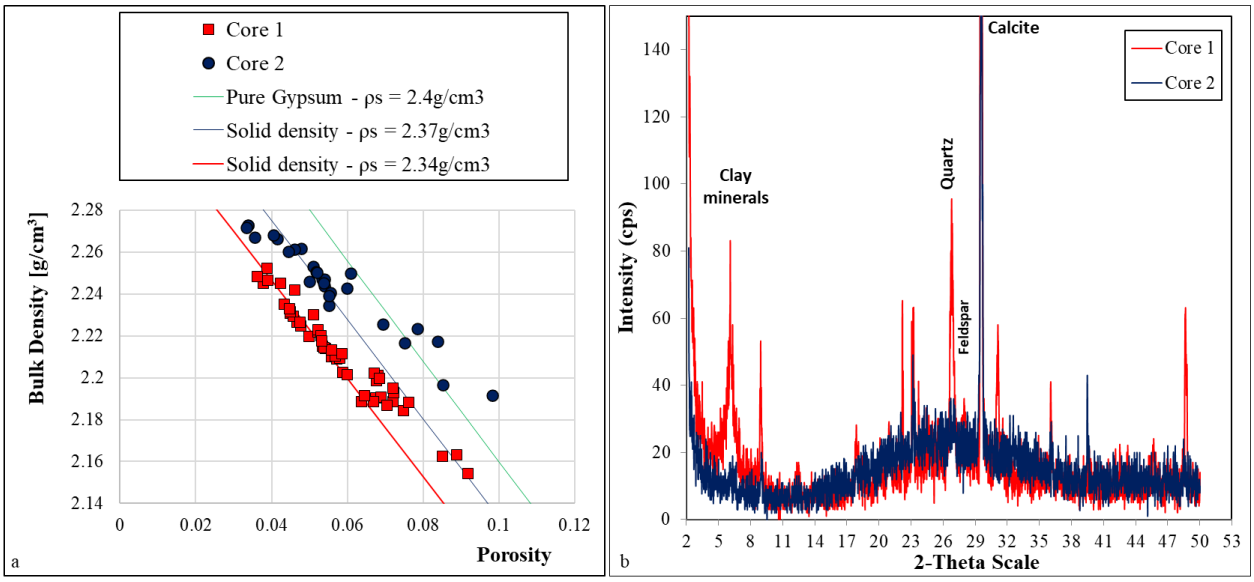

Figure 3. (a) Measurements of porosity against bulk density in the 77 samples, divided on the basis of the starting core (Core 1 – 82.4-82.9 m of depth; Core 2 – 78.0-78.7 m). The low dispersion of the data suggests compositional homogeneity of samples. The lines represent the theoretical value of solid density for pure gypsum (2.4 g/cm^3) and the estimated values of solid density for Core 1 and Core 2 respectively. (b) XRPD analyses of the not-gypsum portion of material from Core 1 (red line) and Core 2 (blue line), showing respectively the abundant presence of clay minerals, in addition to quartz feldspars and calcite, in Core 1 and the prevalence of calcite in Core 2 (Caselle et al. 2022)

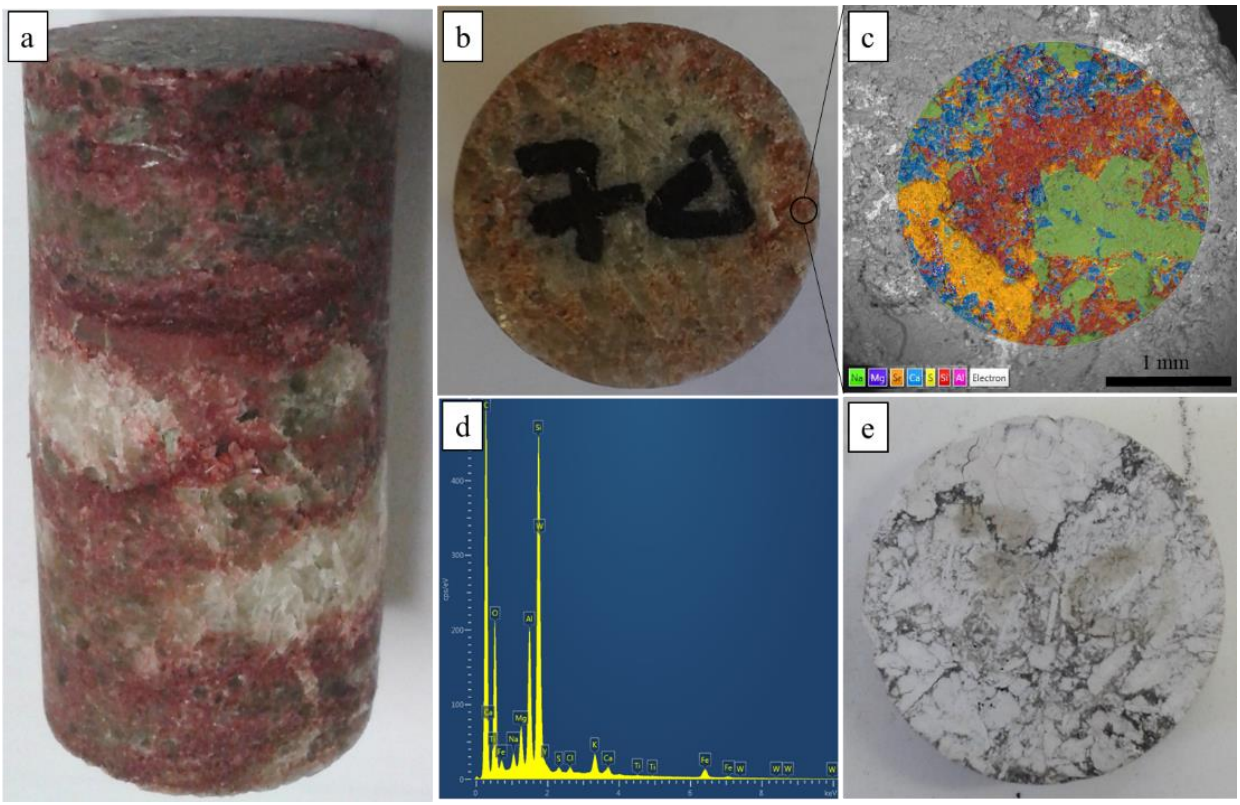

Figure 4. (a) Red discolouration of an oil-saturated sample immediately after a compression test. (b) Red colouration of oil-saturated sample after one month (c) SEM-EDS compositional map. The green portions correspond to gypsum (Ca + S), the orange portions to celestine (Sr + S), blue crystals are carbonate minerals (mainly Ca), while red portions are the thin-grained matrix of the rock (corresponding to main Si and Al, with minor S, Sr and Ca). (d) Punctual SEM-EDS analysis of red portions. (e) Oil-saturated gypsum sample in Figure 4b after heating at temperature of 350°C: gypsum crystals are turned to anhydrite and red portions are turned to black after the expulsion of dearomatized oil.

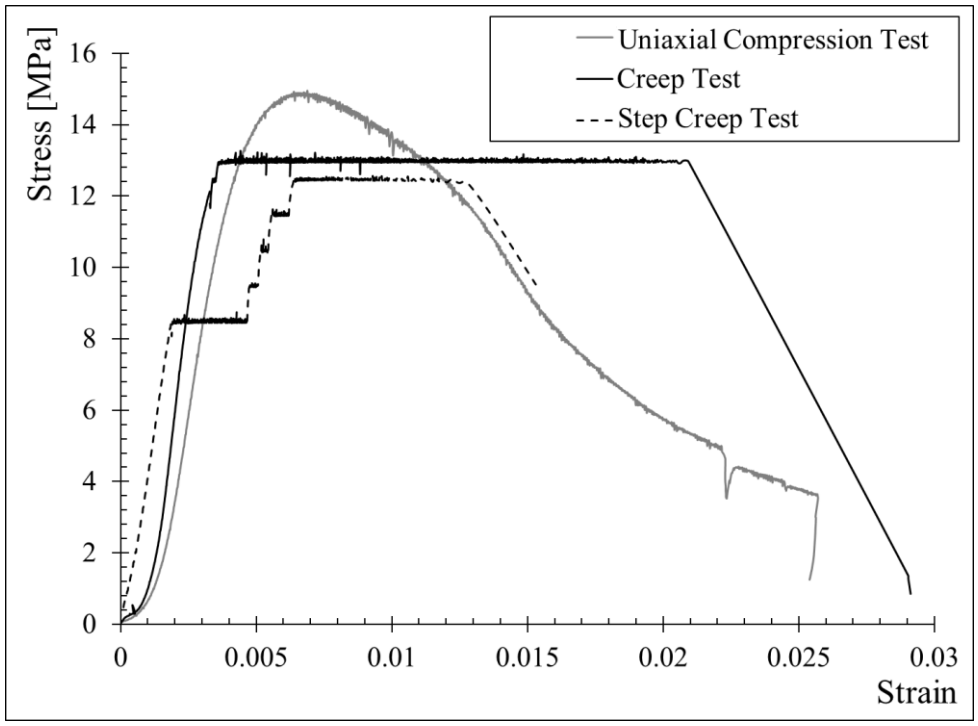

Figure 5. Comparison of typical data for uniaxial compression, conventional uniaxial creep and step creep tests.

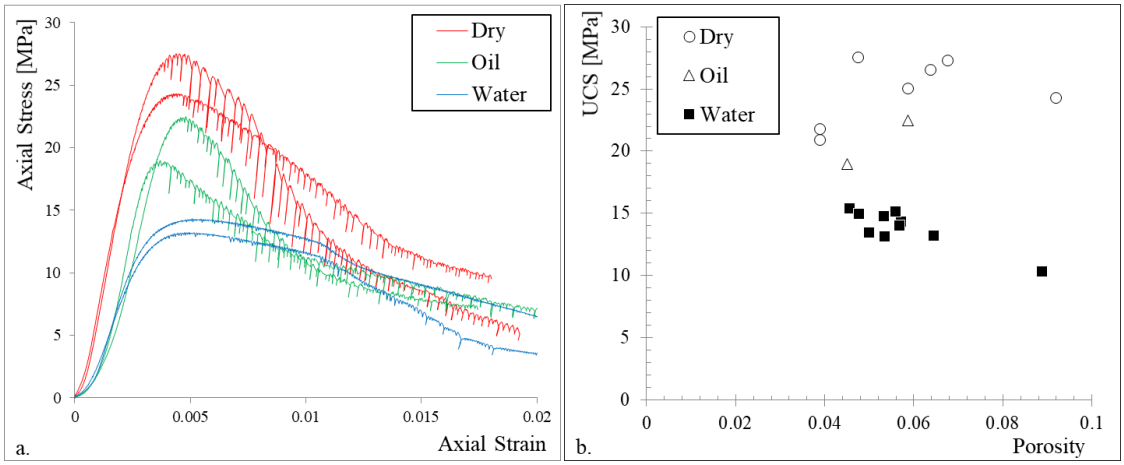

Figure 6. (a) Stress-strain curves of UCS tests on gypsum for dry (red lines), oil-saturated (green lines) and water-saturated (blue lines) samples. (b) UCS as a function of porosity for dry (open circles), oil-saturated (open triangles) and water-saturated (black squares) conditions.

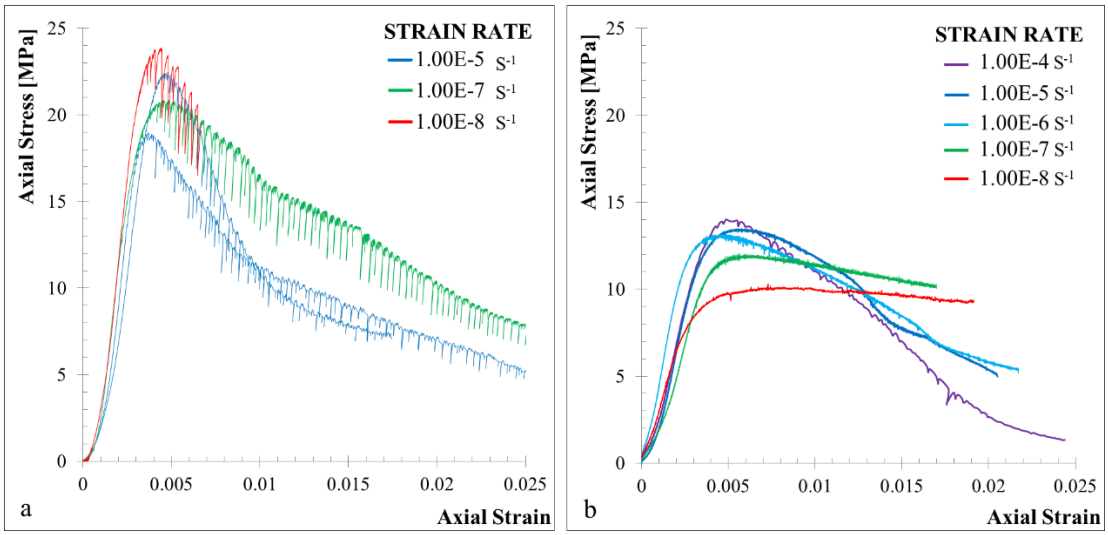

Figure 7. Oil-saturated samples deformed in uniaxial compression with strain rate of 10^{-5}/s (blue lines), 10^{-7}/s (green line) and 10^{-8}/s (red line). (b) Water saturated samples deformed in uniaxial compression with strain rate of 10^{-4}/s (purple line), 10^{-5}/s (blue line), 10^{-6}/s (light blue line), 10^{-7} (green line) and 10^{-8}/s (red line).

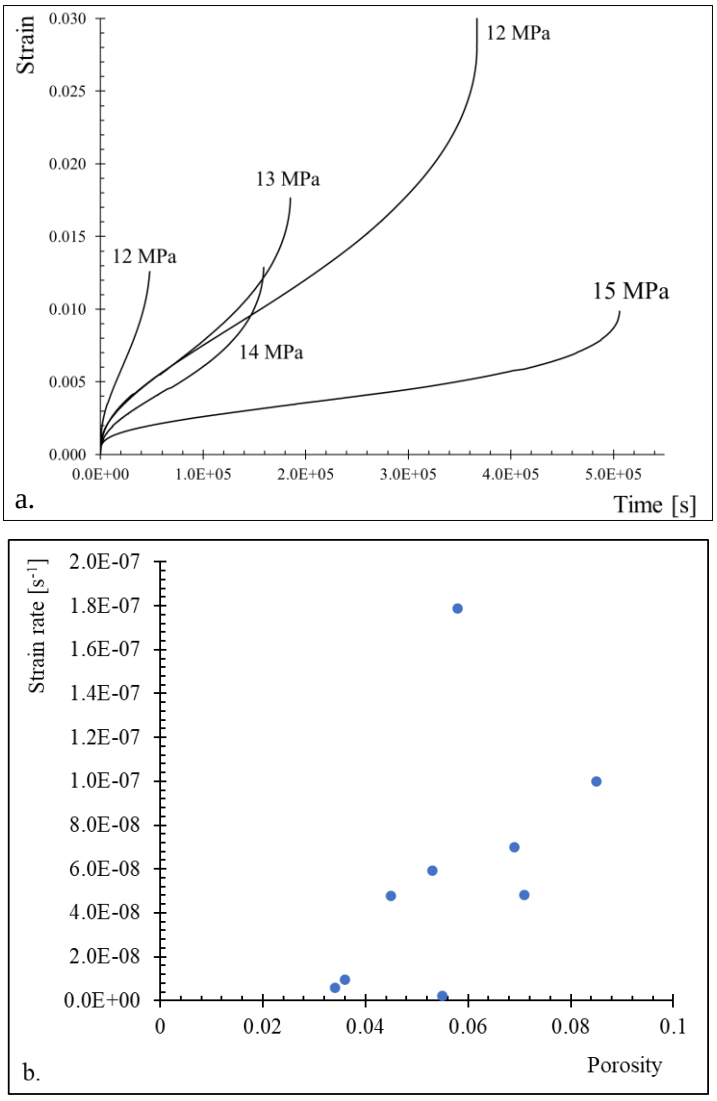

Figure 8. a. Representative strain-time curves obtained from creep tests on water-saturated samples. The applied stress is indicated next to each curve b. Values of strain rate measured in creep tests on water saturated samples against their initial porosity.

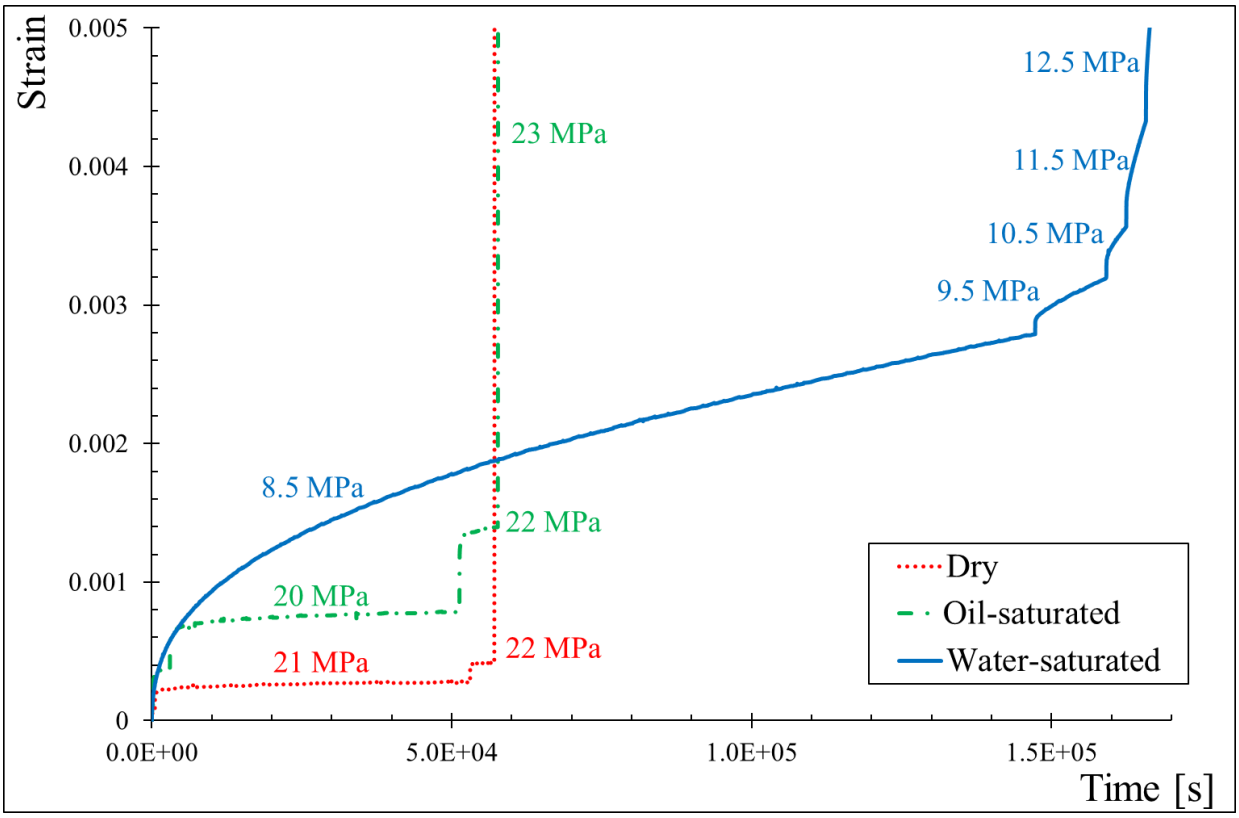

Figure 9. Results of step tests on dry (red line), oil-saturated (green line) and water-saturated (blue line) samples. The stresses applied at each step are reported next to the curves.

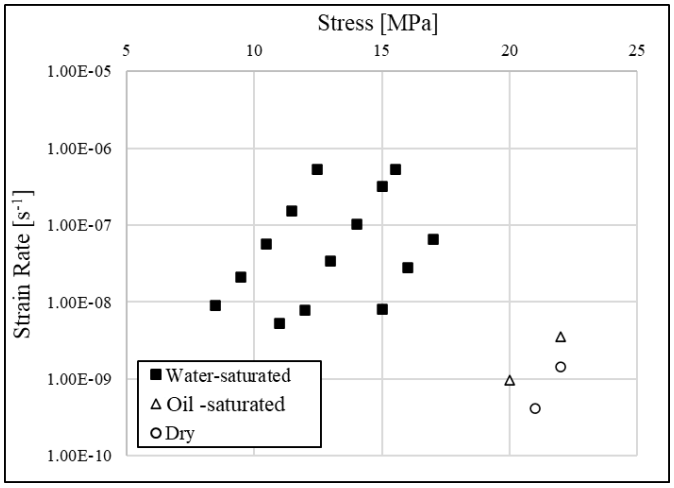

Figure 10. Creep strain-rate as a function of the applied stress for step tests performed on water-saturated (black squares), oil-saturated (open triangles) and dry (open circles) samples.

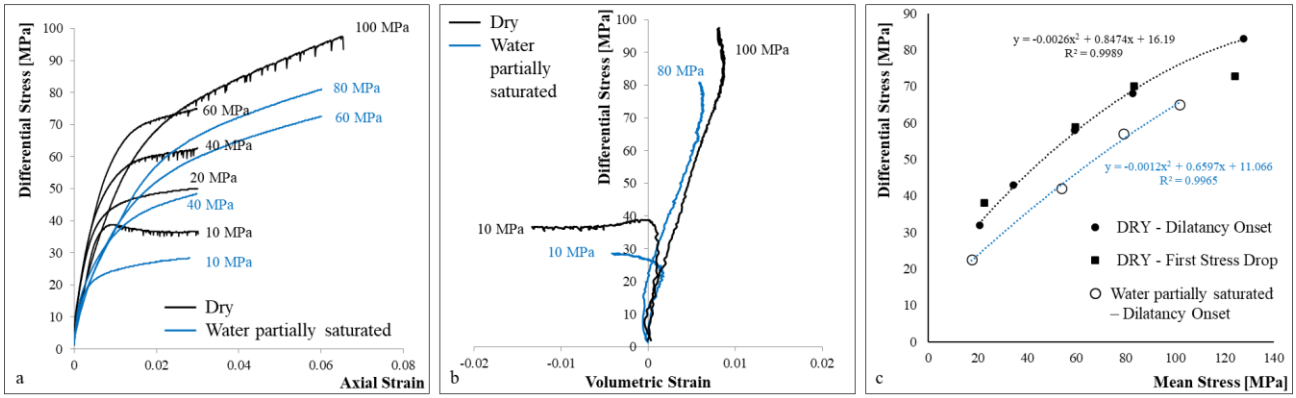

Figure 11. Triaxial data for branching selenite gypsum. (a) Differential stress as a function of axial strain for dry (black) and partially saturated (blue) samples. (b) Differential stress as a function of volumetric strain for dry (black) and partially saturated (blue) samples deformed under the highest and the lowest confining pressure (c) Critical stresses: onset of dilatancy (circles) and first stress-drop in dry conditions (squares). The data are presented in the stress space (differential stress-mean stress) for dry (closed symbols) and wet (open symbols) samples. Failure envelopes are reported in black for dry and in blue for wet samples.

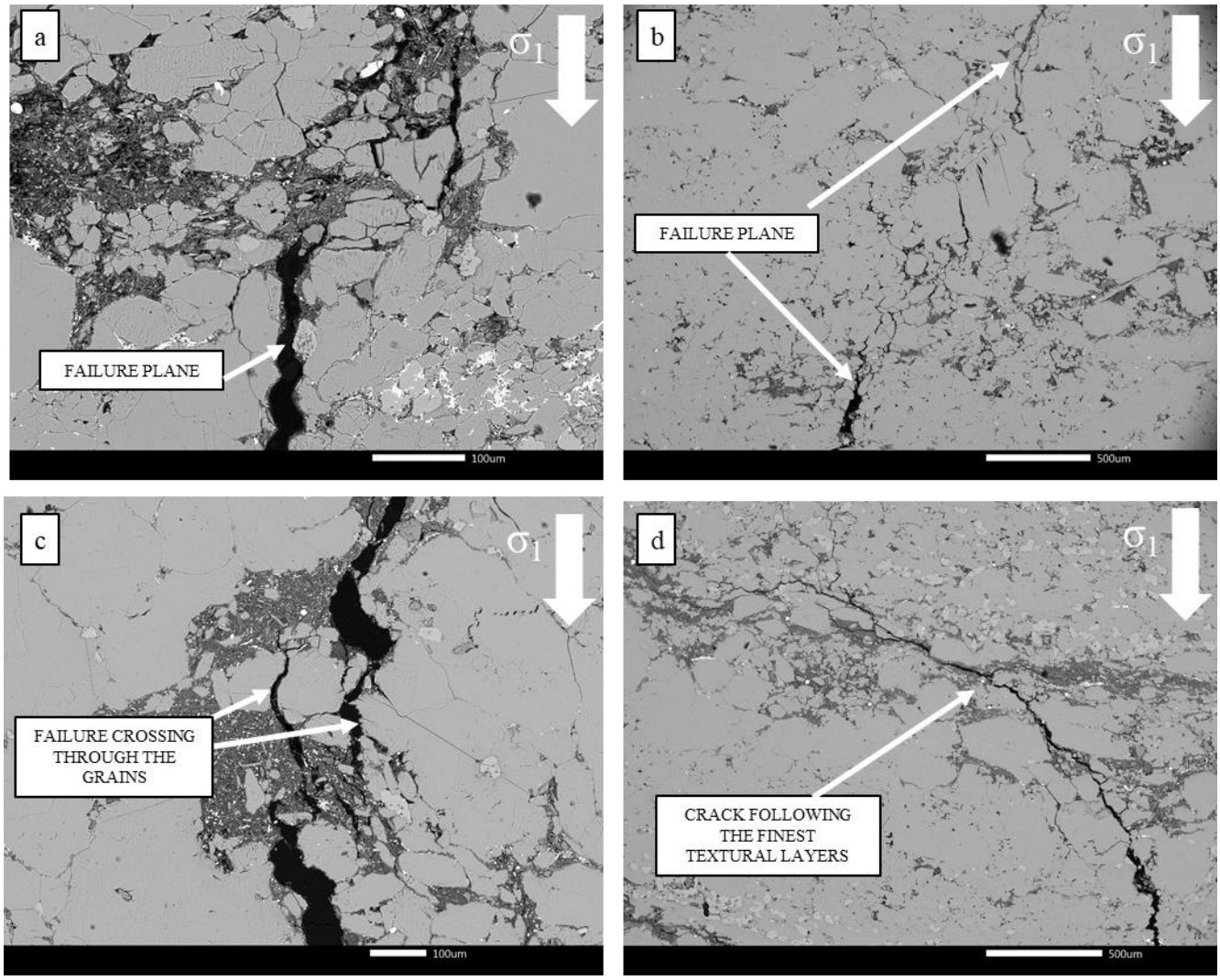

Figure 12 BSE-SEM micrographs of sample deformed uniaxially under dry conditions (sample 34). (a) Failure plane interrupted by changes in microtexture (b) Two crack surfaces, highlighted in the upper right and lower left of the image, that are aligned along a plane but are not continuous in the central portion of the image. (c) Cracks that are interrupted by finer material and cut through gypsum grains (d) Crack following the sub-horizontal layering of the branching selenite structure.

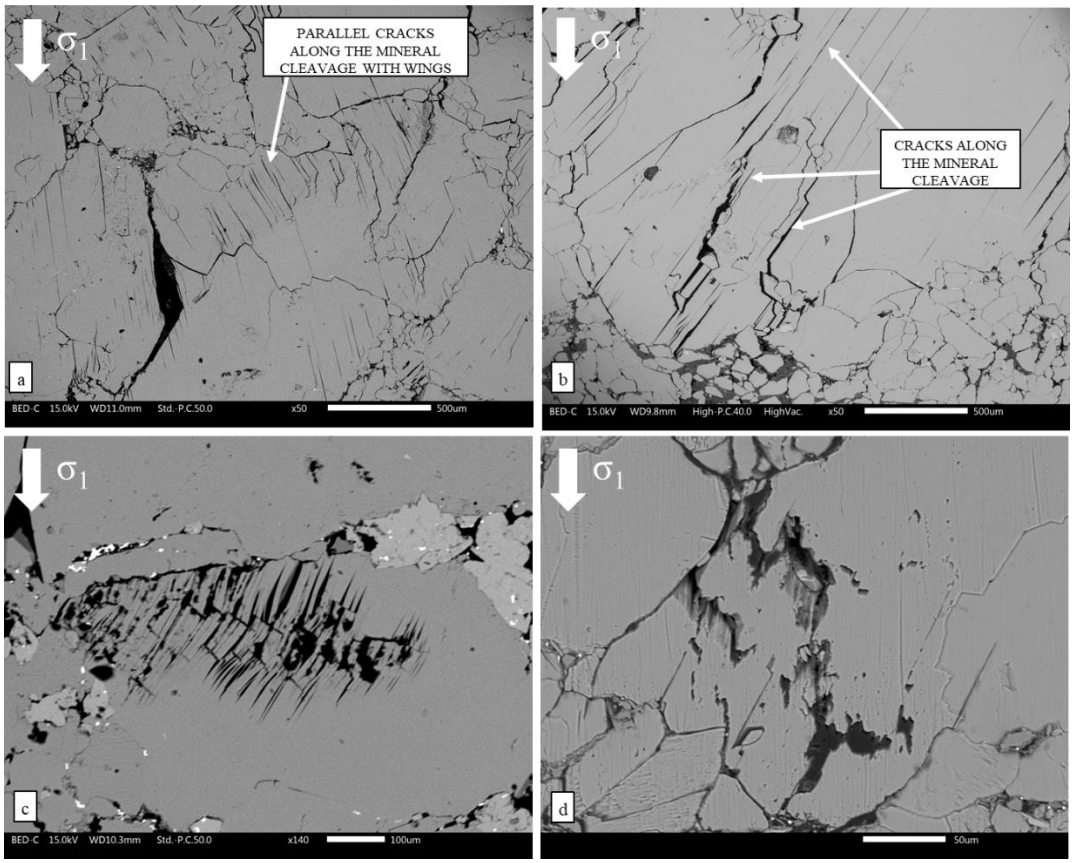

Figure 13 BSE-SEM microstructures of samples deformed uniaxially under wet conditions. Figures show samples 13, 8 and 11, deformed at a standard strain rate of 10-5/s (a and d), slow strain rate 10-7/s (b) and under creep conditions (c), respectively. (a) Gypsum crystal with straight parallel microcracks with wings consistent with the axial direction of the applied stress. (b) Microcracks opening along the gypsum cleavage (c) Intra-crystalline deformation structure, common in slow strain rate and creep samples, that consists of a series of narrow cracks along the mineral cleavage that, being oriented sub-parallel to the axial applied stress, accommodate the strain by the folding of each separated slice and by the creation of short cracks perpendicular to the major principal stress σ_1 (d) Detail of a crack with rounded edges and aperture of 10 to 20 μm that was interpreted as the combined effect of mechanical loading and dissolution.

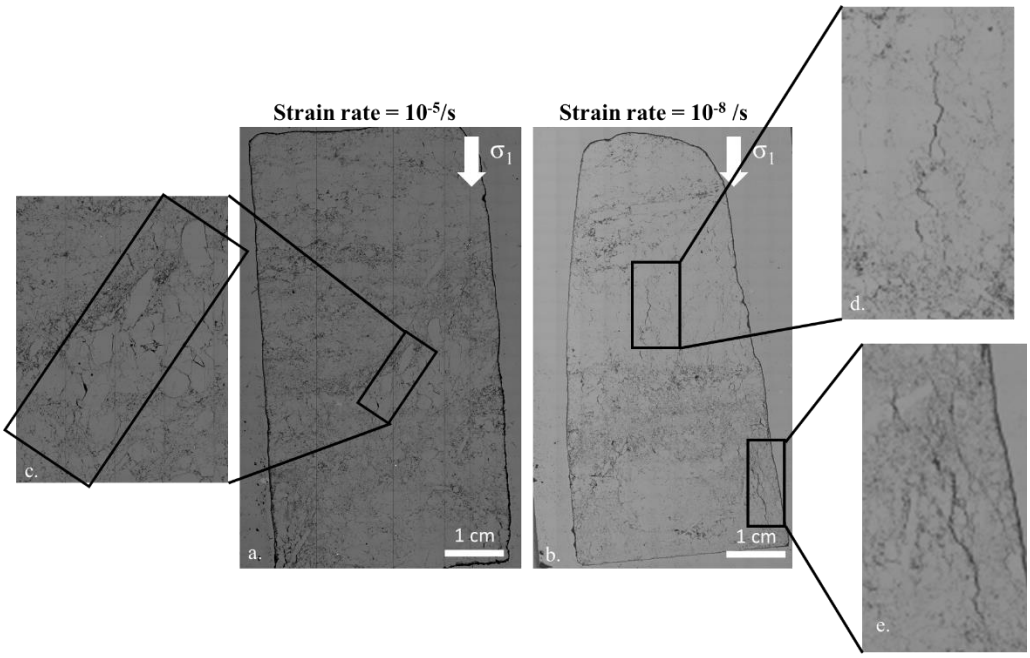

Figure 14 BSE-SEM images of entire thin sections of water-saturated samples deformed uniaxially under strain rates of 10^{-5}/s (a) and 10^{-8}/s (b) (samples 13 and 8, respectively). Magnified images in c., d. and e. highlight the mean orientation of main cracks: with an angle of 30° with respect to the axial load in sample 13 (Figure c) and subvertical in sample 8 (Figures d and e).

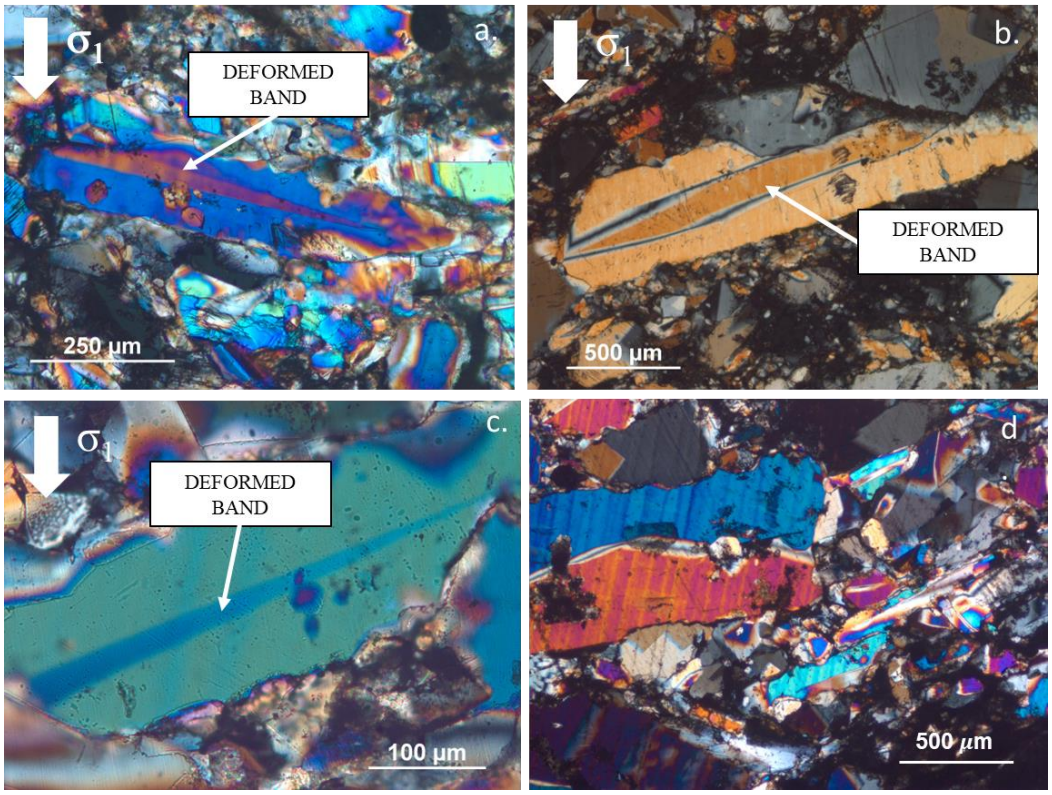

Figure 15 a, b, c. Crossed polar optical microscope images of sample 11 (water saturated, step creep test) showing the presence of deformation bands in the bigger crystals oriented sub-perpendicular to the applied load. d. Example of gypsum crystal in the undeformed material.

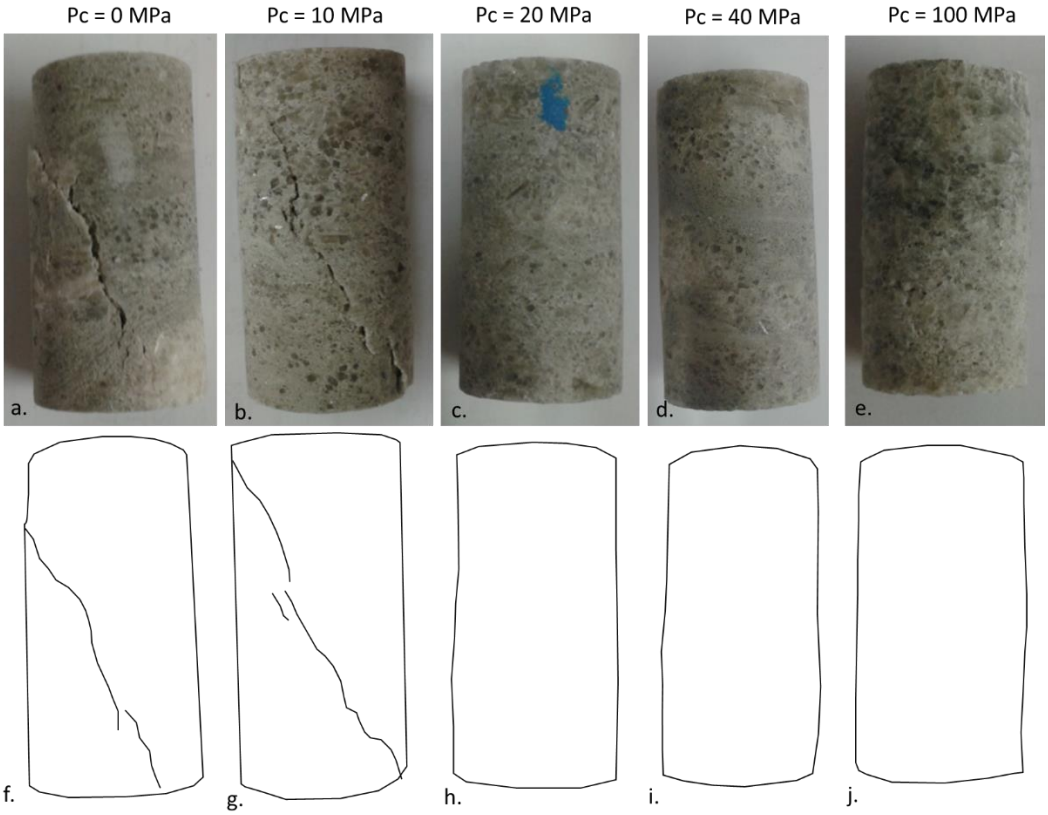

Figure 16 Post-deformation photos of samples deformed under dry conditions (a to e) and outlines of the external shape of the samples and of the main macroscopically visible fractures (f to j).

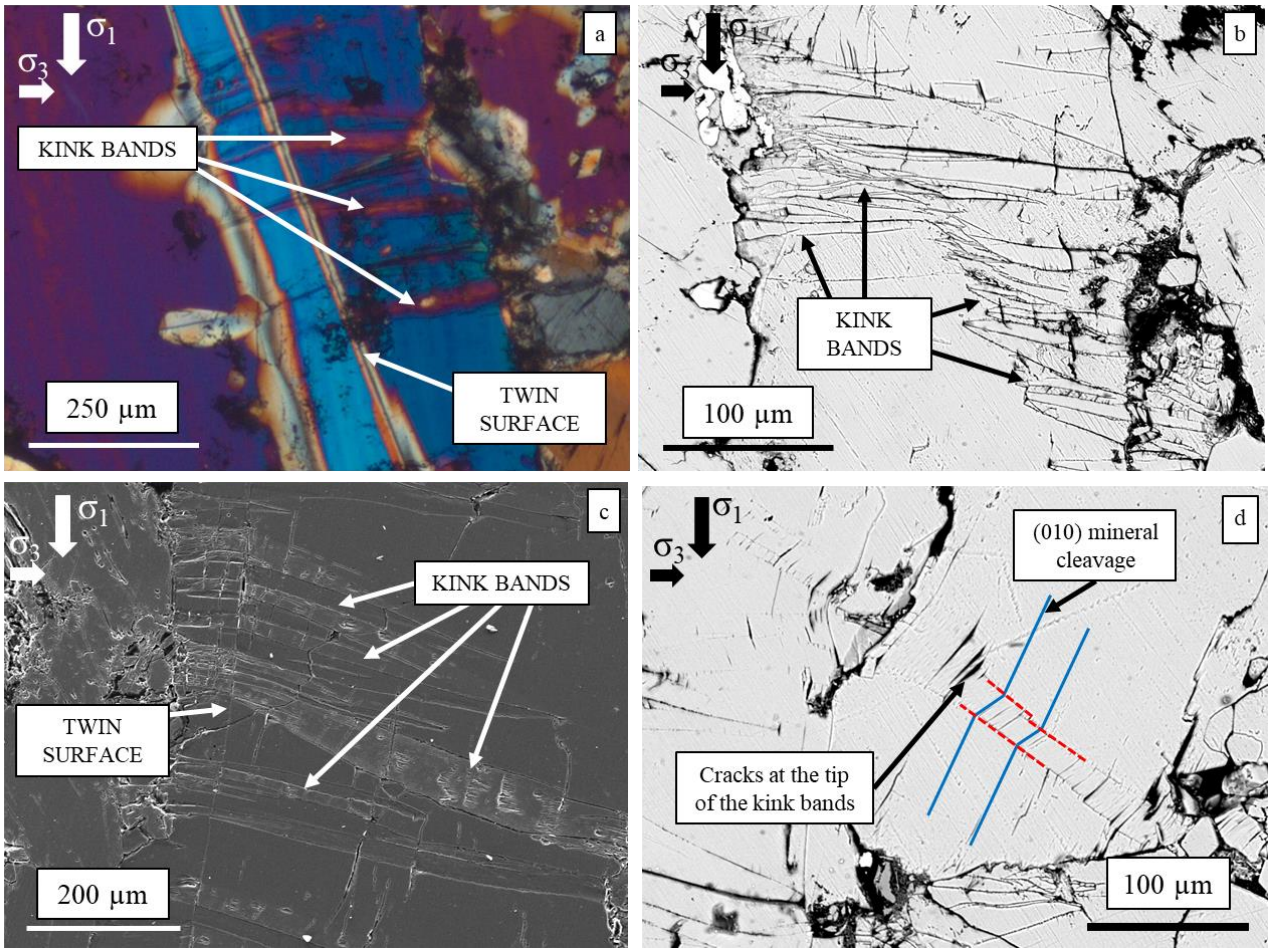

Figure 17 Kinked grains in the microstructures of samples deformed triaxially (samples 28 and 29). (a) Cross-polar optical microscope image of a sample deformed dry with confining pressure of 20 MPa. The twinned gypsum crystal in the image (light blue) is deformed by a series of subhorizontals kink bands: the change of orientation of the crystal leads to in a change in optical properties, resulting in a change of birefringence colour from light blue to purple. (b) SEM-BSE image of a crystal showing intense kink deformation in a sample deformed dry under a confining pressure of 20 MPa. The boundaries of kink bands are clearly marked. (c) SEM-BSE image showing a twinned crystal with subhorizontal kink bands. The sample was deformed wet under a confining pressure of 40 MPa. (d) Detail of a kinked grain. The red dashed lines define the boundaries of the kink band; blue lines are parallel to the mineral cleavage, showing how it is deflected by the kinking deformation. The image, acquired with SEM-BSE, refers to a sample deformed dry under a confining pressure of 20 MPa with stress directions parallel to the black arrows.

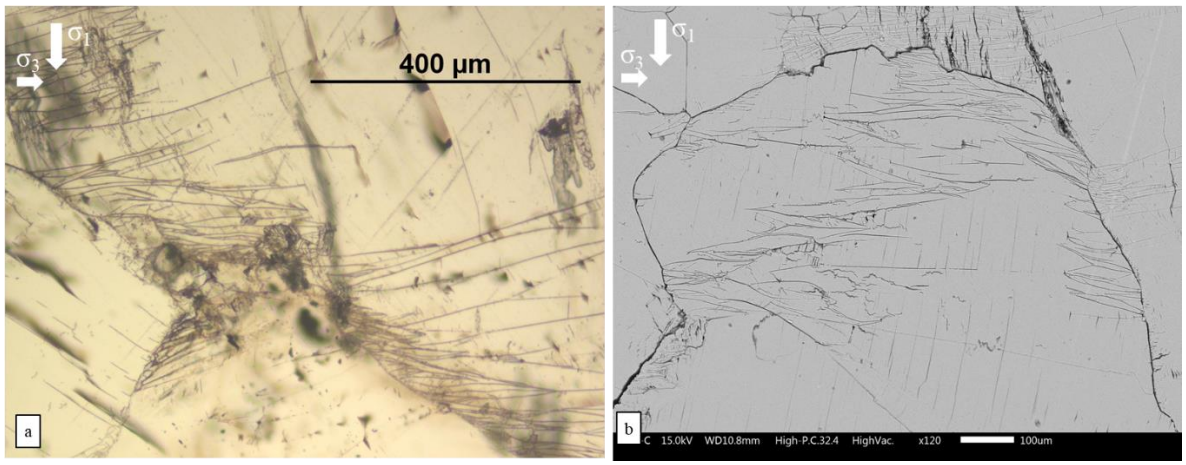

Figure 18 Images of shear bands created by the alignment of kink structures in a sample deformed at a confining pressure of 40 MPa (sample 28). Images were acquired at optical microscope (a) and BSE electron microscope (b).

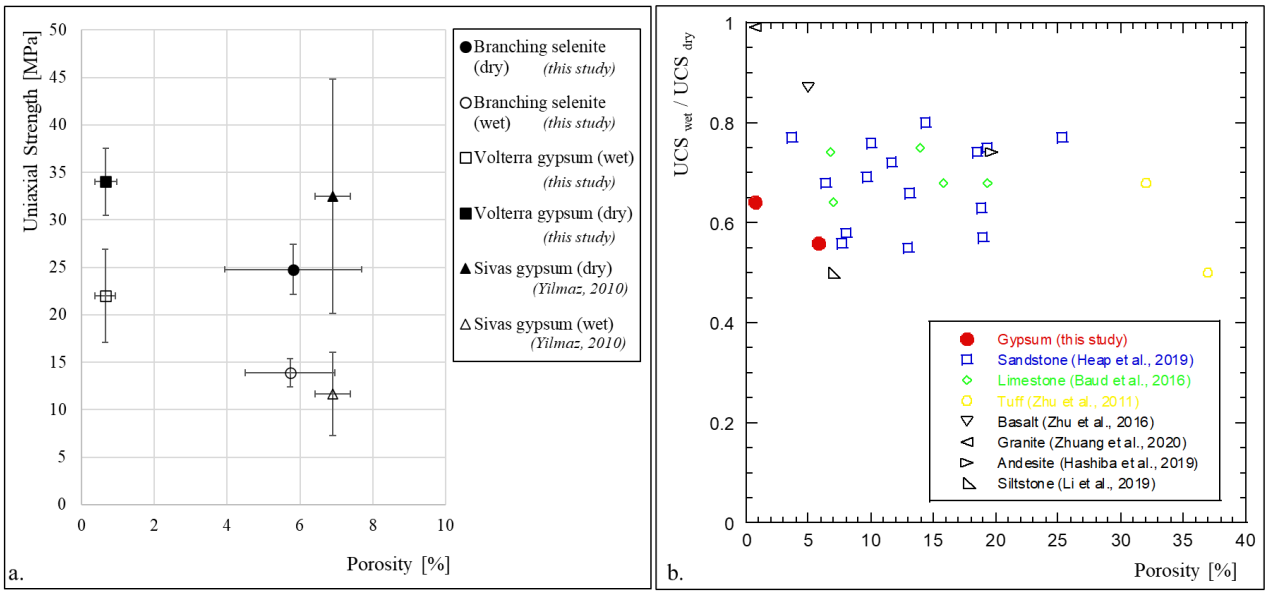

Figure 19. (a) UCS as a function of porosity for branching selenite (circles), Volterra gypsum (squares) and gypsum from the Sivas basin studied by Yilmaz (2010) (triangles). Closed and open symbols are for dry and wet samples, respectively. (b) Ratio of wet UCS to dry UCS as a function of porosity for gypsum (red circles), sandstone (blue squares), tuff (yellow circles), basalt, granite, andesite, and siltstone (black symbols).

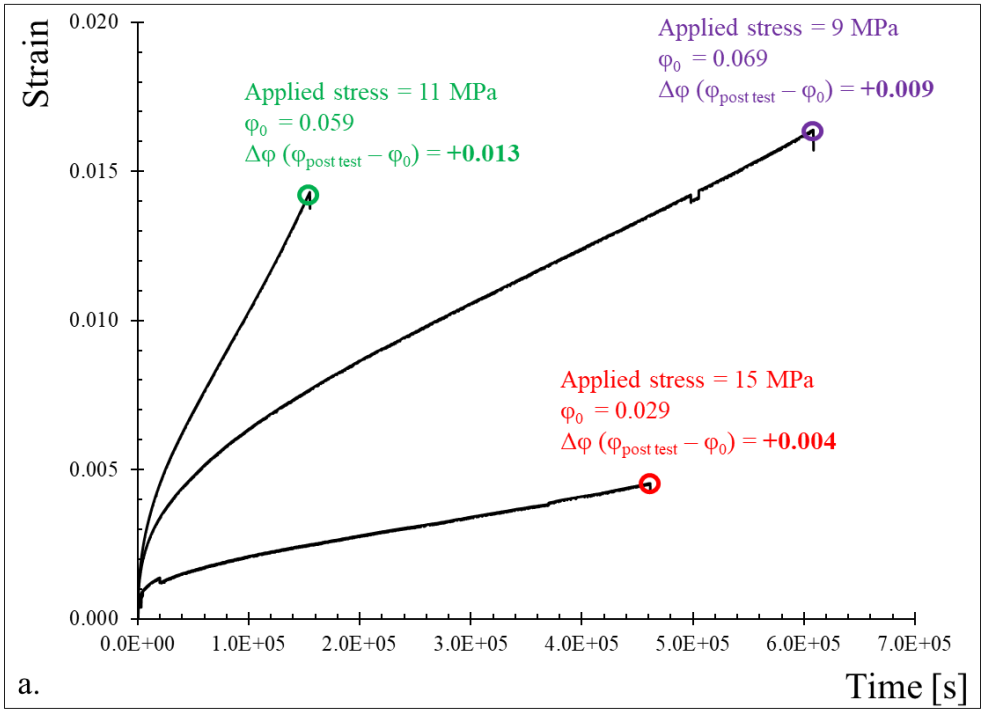

1118

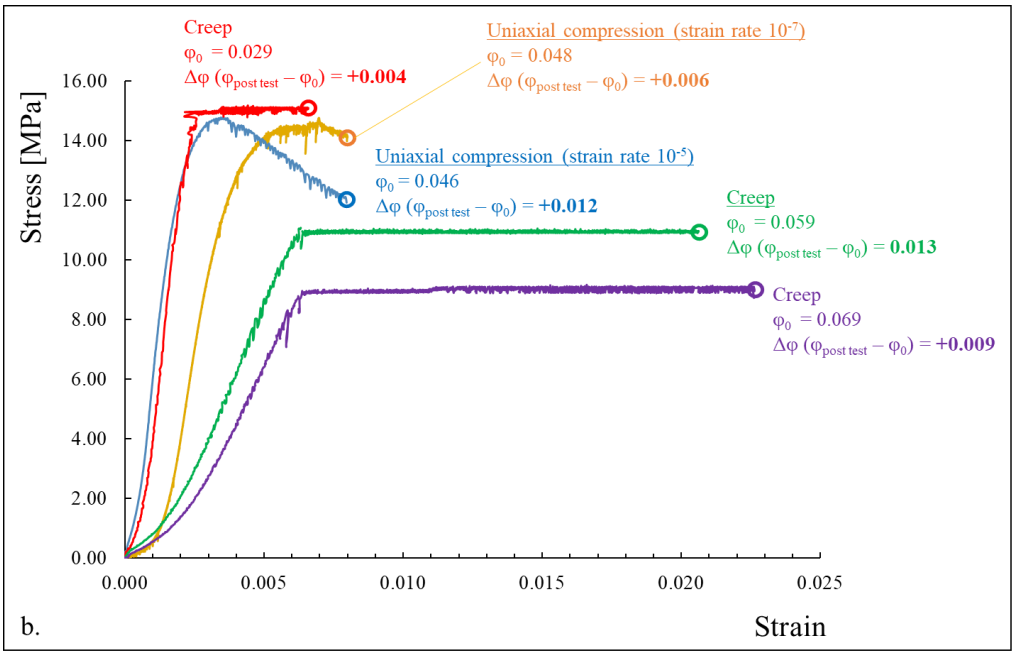

1119

1120

1121

1122

1123 Figure 20. (a) Creep data (strain as a function of time) for targeted experiments on wet gypsum
1124 samples stopped before failure. The initial porosity and the total porosity change are indicated next
1125 to the curves. (b) Comparison between constant strain rate and creep data. Stress is presented as a

function of strain. φ_0 represents the initial porosity of the samples while $\Delta\varphi$ is the difference between the final porosity ($\varphi_{post\ test}$) and the initial porosity φ_0.

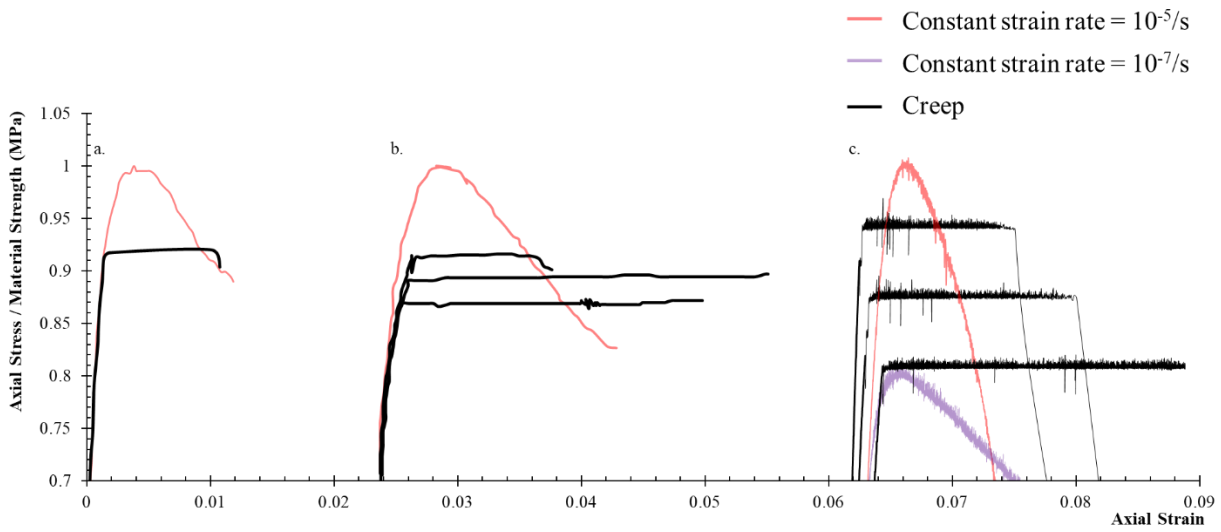

Figure 21 Differential stress as a function of axial strain for a constant strain rate (red) and a creep test (black) on Darley Dale sandstone (Brantut et al., 2014a). (b) Differential stress as a function of axial strain for a constant strain rate (red) and a creep test (black) on Purbeck limestone (Brantut et al., 2014b). (c) Comparison between constant strain rate uniaxial data (red and violet) and creep data on branching selenite gypsum (black). Significantly more strain accumulated during the creep experiments in Purbeck limestone and branching selenite gypsum.

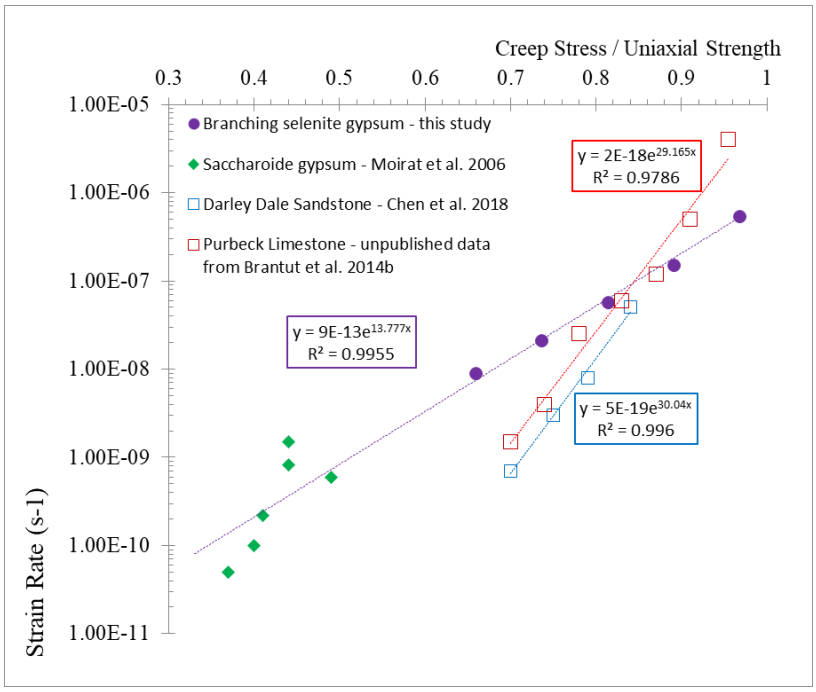

Figure 22 Creep strain rate as a function of the normalized stress for uniaxial creep experiments performed on branching selenite gypsum (violet circles), saccharoide gypsum (green diamonds, Moirat et al., 2006), Darley dale sandstone (blue squares, Chen et al., 2018) and Purbeck limestone (red squares, unpublished data by Brantut et al., 2014b). Exponential fits of the data are also shown.

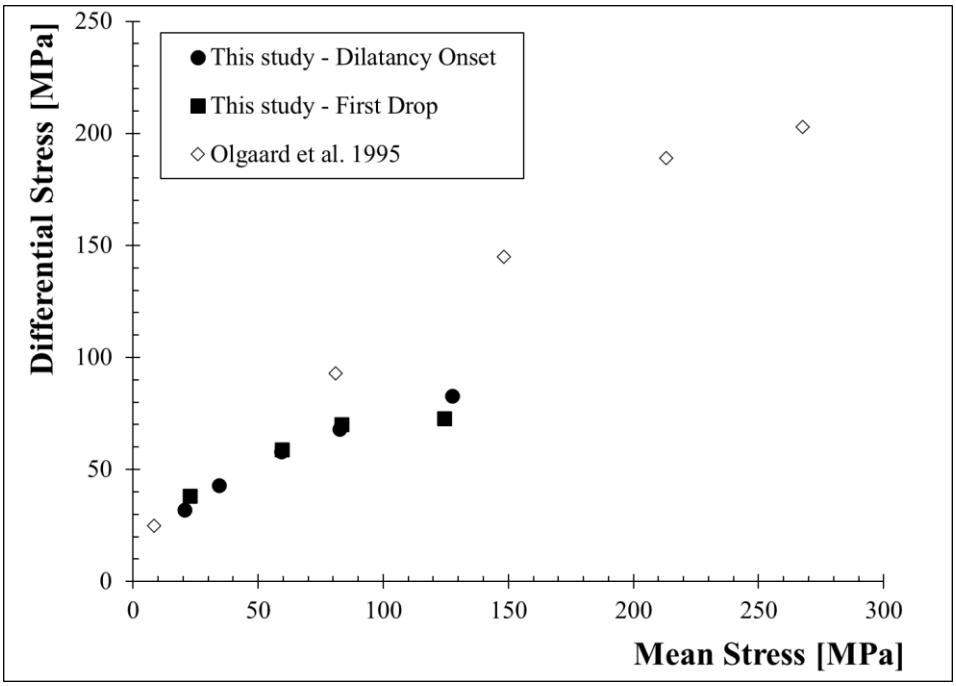

Figure 23 Comparison of the yield envelopes of branching selenite gypsum (black symbols) and of Volterra gypsum (open diamonds) from Olgaard et al. (1995).

1163 Table 1 Test conditions and results of uniaxial compression experiments

Strain Rate s^{-1}	Number of tests	Saturation conditions	Porosity	UCS (range of values) MPa
10^{-5}	7	Dry	0.039 – 0.092	20.92 - 27.52
	2	Oil	0.045 – 0.059	18.97 - 22.48
	7	Water	0.046 – 0.089	10.34 - 15.40
10^{-4}	1	Water	0.057	14.00
10^{-6}	2	Water	0.054 – 0.059	13.15 - 15.15
10^{-7}	2	Water	0.054	12.04 - 14.76
	1	Oil	0.061	20.86
10^{-8}	1	Water	0,060	10.31
	1	Oil	0.060	23.86

1164

1165

1166

1167

1168 Table 2. Summary of conventional and step creep tests performed in this study.

	Saturation	Porosity	Stress MPa	Strain Rate s^{-1}
Creep tests	Water	0.058	12	2E-07
	Water	0.071	12	5E-08
	Water	0.045	14	5E-08
	Water	0.053	13	6E-08
	Water	0.036	15	1E-08
	Water	0.055	8.9	2E-09
	Water	0.034	15	6E-09
	Water	0.069	11	7E-08
	Water	0.085	9.5	1E-07
Step creep tests	Water	0.038	11; 12; 13; 14; 15; 15.5	5E-9; 8E-9; 3E-8; 1E-7; 3E-7; 5E-7
	Water	0.067	8.5; 9.5; 10.5; 11.5; 12.5	9E-9; 2E-8; 6E-8; 2E-7; 5E-7
	Water	0.051	15; 16; 17	8E-9; 3E-8; 6.5E-8
	Oil	0.067	20; 22	1E-9; 4E-9
	Dry	0.042	21; 22	4E-10; 1E-9

1169

1170

1171

1172

1173 Table 3. Summary of the mechanical data for triaxial experiments for dry and partially saturated
1174 samples of branching selenite gypsum.

	Onset Dilatancy		First Stress Drop	
Confining Pressure [MPa]	Mean Stress [MPa]	Differential Stress [MPa]	Mean Stress [MPa]	Differential Stress [MPa]

Dry	10.00	20.67	32.00	22.70	38.10
	20.00	34.33	43.00		
	40.00	59.33	58.00	59.63	58.90
	60.00	82.67	68.00	83.36	70.09
	100.00	127.67	83.00	124.27	72.80
Wet	10.00	17.50	22.50		
	40.00	54.00	42.00		
	60.00	79.00	57.00		
	80.00	101.67	65.00		

1175

1176

1177